Using large-eddy simulation and multivariate analysis to understand the sources of combustion cyclic variability in a spark-ignition engine

Karine Truffin, Christian Angelberger, Stéphane Richard, Cécile Pera

Using Large-Eddy Simulation and multivariate analysis to understand the sources of combustion cyclic variability in a spark-ignition engine

Karine Truffin[a,*], Christian Angelberger[a], Stéphane Richard[a,b], Cécile Pera[a,c]

[a] *IFP Energies nouvelles, 1-4 avenue de Bois-Préau, 92852 Rueil-Malmaison, France*
[b] *TURBOMECA, avenue Joseph Szydlowski, 64511 Bordes, France*
[c] *Infineum UK Ltd, Milton Hill, Abingdon OX13 6BB, England*

Abstract

The origins of cyclic combustion variability (CCV) in spark-ignition engines are investigated using Large-Eddy Simulation (LES) of a stable (low CCV) and two unstable (high CCV) operating points of a specifically dedicated experimental test-rig set up around a four valve pentroof single cylindre spark-ignition engine fueled with a premixture of gaseous propane and air. The unstable points are obtained from the reference by reducing significantly the equivalence ratio and by an important dilution by nitrogen respectively. A LES methodology is proposed and shown to be able to reproduce the experimental findings concerning phase-averaged mean and statistical variations around it of a number of key engine combustion parameters. The CCV and factors causing it are first illustrated by comparing typical slow and fast burning cycles in combination with simple correlation plots of major engine parameters, this allows qualitatively showing how local and global sources concur to generate CCV. In a second step, single parameter and multivariate regressions build from the LES results allow quantifying the relative importance of different local and global CCV sources. Finally, the comparison of the obtained findings as to the relative importance of major parameters on CCV are compared with qualitative summary from an extensive experimental survey by Ozdor et al. The presented LES results overall confirm

*Corresponding author. Tel: +33147525412, Fax: +33147526685. E-mail address: karine.truffin@ifpen.fr

major findings from the survey, but also indicate that detailed causes of CCV depend on the type of engine and its operation.

Key words: Large-Eddy Simulation, Cyclic combustion variability, spark-ignition engine, turbulent combustion, multivariate analysis, correlation

1. Introduction

The operation of spark-ignition engines (SIE) is characterised by a non-repeatability of instantaneous combustion rate between different cycles at nominally identical engine operating conditions, commonly referred to as cycle-to-cycle variation [1, 2] or cyclic combustion variability (CCV). CCV inevitably appears over the whole engine operation range, due in particular to the unsteady, cyclic and turbulent nature of flow and combustion in SIE. It is common practice to consider that a CCV amplitude (measured in terms of standard deviation of Indicated Mean Effective Pressure (IMEP), normalised by its mean value) of less than around 5 % is acceptable [3]. As long as the CCV amplitude is sufficiently small, engine simulation softwares can predict with sufficient accuracy combustion using statistical approaches as RANS (Reynolds-Averaged Navier-Stokes) that neglect cyclic variations and aim at reproducing a phase averaged, statistically most probable, cycle. For higher CCV amplitudes however, individual cycles will behave very differently from this statistically most probable cycle. As a result, predictions of fuel consumption or emissions over a number of cycles may differ quite substantially from the one based on the mean engine cycle. These differences increase with the CCV amplitude and may reach extreme levels in the case of misfires or extreme knocking cycles [4, 5].

In a context of increasingly stringent constraints on fuel consumption, CO_2 production, and pollutant emissions from road transport, it becomes crucial to be able to predict and control individual engine cycles, and thus to address the occurrence and effects of CCV. Engine technologies as downsizing [6, 7], direct injection (DI) [8] or controlled auto-ignition (CAI) [9, 10] are examples of technologies presently explored in order to reduce the CO_2 emissions from

future SIE. Yet the occurrence under certain operating conditions of excessive CCV when implementing these technologies is one of the factors limiting their practical performance or range of operation. Being able to predict CCV in early design phases based on an improved knowledge of their sources and effects could effectively contribute exploiting the full potential of these promising SI technologies under real operation.

The understanding of how the complex combination of different sources leads to the occurrence of CCV for a specific engine design or mode of operation is still limited. CCV is indeed the result of a complex combination of different flow phenomena. These phenomena can be classified into two main categories, depending on the related spatial and temporal scales:

- Global phenomena [11, 12], which are related to global operating characteristics: trapped mass, intake mass flow rate, tumble ratio, overall equivalence ratio, mean cylinder pressure, mean intake charge temperature, exhaust gas recirculation (EGR) rate, etc. Their spatial scales are of the order of some characteristic dimension of the engine, and their time scales of the order of the crank angle and up to the duration of an engine cycle;

- Local phenomena [13, 14, 15], which are related to local flow variables: temperature, pressure, mixture composition, turbulence, flow velocity, strain rate, etc. Their spatial scales range from some micrometers up to some millimeters, their time scales from some microseconds up to the crank angle.

Both scales can exhibit cycle-to-cycle variations and do strongly interact, making the understanding of CCV complex. This is especially true in the combustion chamber, where the non-linear response of combustion is a key contributor to CCV.

Experimental studies [11, 12] certainly allow identifying CCV for a given engine concept, and they can help testing control strategies to limit its occurrence and impact. Aleiferis [16] conducted research on a pent-roof single-cylinder port

fuel injection engine fueled with a stratified mixture of iso-octane/air. He concluded that the flame area was highly correlated to the crank angle at which 5 % fuel mass fraction was burnt, while the flame volume was highly correlated to spark energy. In a recent paper [3] the impact of the ignition system on the combustion in a direct-injection engine was studied, showing that larger spark gaps, longer spark life durations and multi-spark ignitions were beneficial to the extension of the dilution limit and to the combustion stability. Such experiments only come into play once a prototype has actually been built, in design phases where modifications to the basic concept are difficult to achieve because of cost and time constraints. Furthermore, the achievable understanding is limited by the impossibility to have access to all necessary thermodynamic and flow quantities on an instantaneous, cycle resolved basis. Nevertheless this is required to gain a basic understanding of the sources of CCV. The understanding gained from such studies is thus only partial and rarely valid beyond the specific studied case.

Large-Eddy Simulation (LES) is a 3D-CFD technique that has the potential to address the numerous coupled phenomena influencing engine combustion, and potentially gives access to any quantity needed to understand and characterize CCV. Its ability to deal with turbulent flows [17, 18, 19, 20] and reactive flows [21, 22, 23] in SI engines has been demonstrated. But only a few LES studies were dedicated to the prediction of CCV [24, 25, 26] using either the Thickened Flame (TFLES) [27], or the Extended Coherent Flame (ECFM-LES) [28, 29, 30] turbulent combustion models and the AVBP code[1] [31, 32]. Vermorel et al. [26] have applied the LES models developed by Richard et al. [28] to explore the origins of CCV in an SIE fueled with gaseous propane using AVBP. They have demonstrated that computing 10 consecutive complete four-stroke engine cycles allowed reproducing experimental findings on CCV. They also illustrated how analysing this LES could be used to identify sources of CCV. In the studied case they were found to be stochastic in nature and

[1] http://pantar.cerfacs.fr/4-26334-The-AVBP-code.php

related to the turbulence of the intake flow, and its coupling to spark-ignition and flame propagation. Lacour & al. [33] have acquired the SGEmac experimental database dedicated to a detailed study of CCV in an optical access single cylinder SIE fueled with a homogeneous mixture of propane and air. Low CCV operating points were acquired in order to fully characterize the engine and allow model validation. Two operating points were then explored in order to characterize high CCV values resulting either from an important dilution by nitrogen of the fresh gas mixture (EGR emulation), or by reducing the fuel/air equivalence ratio. Available data comprise crank angle resolved measurements of pressures and temperatures at different locations in the engine set-up, as well as visualisations of velocities and combustion progress using optical diagnostics. This database has served for validating the prediction of CCV using LES. In [34], LES of the flow under motored (without combustion) conditions were performed with AVBP and were shown to yield an accurate reproduction of the flow field inside the combustion chamber and of the acoustics in the intake and exhaust ducts. In [24] and [25] the same numerical set-up around AVBP was used for LES of fired operations. The simulation of 25 consecutive full cycles of the stable and 50 cycles of an unstable operating point in [24] using the TFLES combustion model [27] demonstrated the ability of the employed LES approach to quantitatively predict the CCV levels observed experimentally. Qualitative analysis of the LES was performed to understand the causes for incomplete combustion which occurred in some cycles of the high-CCV case, but no quantitative analysis was proposed that could have allowed correlating CCV with global or local phenomena.

The present work aims i/ at complementing these studies of CCV with an alternative LES methodology based on AVBP, ii/ at both reproducing experimentally observed CCV in the SGEmac engine, and iii/ at proposing a systematic way to explore and quantify its sources. While the above mentioned studies were based on simulating the whole engine set-up with LES, the computational domain including the whole intake and exhaust lines between the intake and exhaust plena, the present work is based on an alternative LES methodol-

ogy [35], exploiting system simulation of the intake and exhaust ducts to impose unsteady boundary conditions for the LES of the combustion chamber and its immediate neighborhood. Furthermore, premixed combustion is addressed using ECFM-LES [26, 28], a LES formulation of the widely used Coherent Flame Model.

The objective of the present work is threefold:

- apply the LES methodology developed and validated for motored operation in [35] to fired operation based on the ECFM-LES combustion model, and demonstrate its ability to reproduce experimentally observed CCV levels;
- acquire a basic understanding of the origins of CCV and of their impact, as a result of both global and local phenomena;
- propose a systematic method for analysing LES of CCV in order to identify major parameters affecting it, and providing a quantification of their relative importance.

Section 2 starts by describing the experimental set-up and main characteristics of the SGEmac engine. Section 3 then details the numerical set-up of the LES of the SGEmac engine, and gives key elements of the proposed LES methodology. A first validation of the latter is provided in Section 4, which compares LES predictions of phase-averaged cylinder pressure and its variability for the reference low-CCV (or stable) operating point with experimental findings. Section 5 then presents the reproduction of experimental CCV findings for two high-CCV (or unstable) operating points of the SGEmac database achieved with the developed LES methodology. A first investigation of the CCV origins is proposed based on the visualisation of the flame propagation and by examining the degree of correlation between IMEP and the different combustion and flow characteristics. Finally, a multivariate regression model built from LES results, allows to quantify the relative importance of different local and global CCV sources and classify the degree of importance of several phenomena acting

on CCV.

2. The SGEmac single cylinder engine experiment

The SGEmac engine test bench [33] was specifically designed to allow a detailed validation of the ability of LES to predict CCV. It consists of a single cylinder spark-ignition engine equipped with a 4-valve pentroof combustion chamber and with a flat piston. The main engine characteristics are summarised in Table 1. The whole SGEmac set-up [24] includes: (1) an intake plenum to which air is fed via a sonic nozzle in order to perfectly control mass flow; (2) a mixing plenum into which gaseous propane is injected far upstream the combustion chamber for creating a perfect reactive pre-mixture; (3) the combustion chamber with multiple optical accesses; (4) an exhaust plenum in order to perfectly control and define boundary conditions. The volumes of both plena were chosen sufficiently large to damp acoustic perturbations.

The characteristics of the three simulated operating points from the SGEmac database [33] are summarized in Table 2. The stab_ref operating point is the stable reference point at stoichiometry with no external dilution. The unstable operating points unstab_dil and unstab_lean result from respectively diluting the fresh gases with additional N_2, and air (by reducing the fuel/air equivalence ratio). Both of these unstable points were defined in order to keep the mean indicated effective pressure (IMEP) as close as possible to that of stab_ref, resulting in necessary adaptations of the spark timing.

3. LES methodology

3.1. Numerical approach

The present LES were performed using the parallel AVBP solver [31, 32] which is dedicated to the simulation of reactive unsteady flows and explicitly solves the compressible multi-species Navier-Stokes equations on unstructured meshes with a cell-vertex finite-volume formulation. A second order centered Lax-Wendroff convective scheme is used in this study, in combination with an

explicit time-advancement in an attempt to achieve a reasonable compromise between stability and numerical dissipation [36].

3.2. Computational domain and boundary conditions

In order to avoid simulating the full engine set-up using LES, the methodology developed in [35] was adopted. First, a sketch of the full engine set-up is built and simulated using the IFP-Engine system simulation (or 1D CFD) library [37, 38] within LMS-Imagine.Lab solver. From this system simulation, crank-angle resolved pressure and temperature evolutions at the locations corresponding to the boundaries of the 3D computational domain are extracted, and prescribed as boundary conditions for the LES. Species mass fractions of the gaseous mixture of air and propane are also imposed. Only one-way coupling between the system simulation and LES is hereby accounted for, so that no feedback from the LES to the system simulation is addressed. As the cyclic variability of the flow in the intake and exhaust ducts had been experimentally shown to be very small [33], the same time evolutions of pressure and temperature were imposed for all simulated, consecutive LES cycles.

At the intake and exhaust boundaries, a multi-species extension [36] of the Navier-Stokes Characteristic Boundary Conditions (NSCBC) [39] were imposed via a linear relaxation method (LRM) [40]. This method allows separating waves entering and leaving the domain, thus minimizing spurious reflexions at the boundaries. The cut-off frequency of this low-pass filter is directly proportional to a relaxation coefficient that ensures that the imposed pressure relaxes towards the target time signal coming from system simulation. Finally a mixed inflow /outflow formulation was selected in order to handle the occurrence of flow reversals during certain phases of the engine cycle, a nominal inflow becoming an outflow and vice versa. To this purpose, the boundary conditions are switching from an inlet to an outlet formulation according to the instantaneous direction of the local flow velocity.

Fig. 1(a) shows the extent of the computational domain used in the LES, comprising the combustion chamber and its immediate neighborhood. During

fired operation, hot burnt products from the combustion chamber can be pushed back into the intake ducts and reach the inflow boundary if a too short portion of the intake duct is included in the LES. In order to avoid numerical problems resulting from the composition change at the boundary, 1D CFD results were used to estimate the backflow distance, the length of the intake duct included in the mesh was set to 70 mm. The outlet boundary conditions was set at the location of an experimental pressure sensor at the junction of the two exhaust ducts coming from the cylinder. No attempt was made to impose turbulent flow conditions at the inflow boundaries of the LES domain. As a consequence of the reciprocating nature of the engine, the flow inside the intake and exhaust ducts is strongly oscillating, even during the closed valve phases. Therefore, the turbulent flow inside the ducts cannot be considered as corresponding to a fully established duct flow, despite the high flow Reynolds numbers and the important duct lenghts. Any attempt to impose realistic turbulent flow patterns on inflow boundaries would therefore be a complex task, that would require a detailed study of the unsteady 3D flow in the engine ducts. In the present LES, turbulence in the ducts was therefore only a result from the shear generated by the wall boundary layers. Neglecting inflow turbulence appears all the more justified as the key flow feature responsible for turbulence during combustion is the strong flow detachment generated around the valves during intake that induces a tumbling flow, the compression of which by the piston ultimately leads to small scall turbulence. An estimation of the time scales of any turbulence entering the cylinder from the ducts shows that they are much shorter than the duration of the compression phase. Such turbulence is therefore dissipated very fast during intake and does not have any impact on combustion. The obtained accurate predictions of the tumbling flow and its compression in the present LES a posteriori justify this simplifying assumption. Convective wall heat transfer was modeled using a logarithmic law of the wall as described in [41] using the Diwakar model [42], which was specifically dedicated to the prediction of wall heat flux in spark-ignition engines. Finally, the spark plug was not discretized in the present simulations. This appeared justified as the electrodes protrude

very few into the combustion chamber. Attempts (not shown here) to account for the spark plug in the computational mesh demonstrated that this does not fundamentally affect conclusions drawn on the on-set and early development of combustion described in the present paper.

3.3. Moving mesh management

The engine cycle is divided into 41 mesh phases, each characterized by a constant connectivity, which changed from phase to phase to adapt to the important displacement of the piston and valves. Each mesh phase contains an initial and a final grid generated before the simulation using an external grid generator. Within a mesh phase, the position of each node is interpolated in time and space between its initial position in the initial mesh and its final position in the target mesh. The quality of the deforming tetrahedral mesh is controlled through mesh smoothing [43]. In order to restrict the grid deformation while maintaining enough spatial resolution, a second-order interpolation is used [44]. Fig. 1(b) illustrates the achieved discretisation of the computational domain. In the present computations, the grid deformation maintains an average spatial resolution close to 0.7 mm in the cylinder during the engine cycle, with down to 0.2 mm around the spark plug position and during combustion, as well as in the valve curtains. The smallest cell sizes of 0.04 mm are used for the residual valve lift of 0.35 mm. From the cylinder-head outwards into the ducts, meshes are gradually coarsened, largest cells sizes in the ducts reaching values of about 4 mm. The smallest grid is found at TDC and consists of 2 million tetrahedral cells, while the largest grid of 8.2 million tetrahedral cells is found at the intake BDC.

3.4. Sub-grid scale modelling

Unclosed sub-grid stresses in the momentum equations are modeled using the Sigma model [45]. It is specifically designed so that turbulent viscosity vanishes in different canonical laminar flows (pure shear, pure rotation, isotropic expansion and contraction, stagnation point) for which no sub-grid scale (sgs)

activity is expected. This model also properly propagates a vortex ring along the wall after the impingement of a pulsating jet [46], a phenomenon commonly encountered in piston engines.

The ECFM-LES turbulent premixed combustion model [26] is used to describe the flame front propagation. It combines two approaches: first, the CFM-LES model [28] is an adaptation of the original CFM model [30, 47] to LES, based on a transport equation for the filtered flame surface density (FSD) $\overline{\Sigma}_c$. Second, ECFM [48] is an extension of the CFM model to allow the description of the turbulent combustion of stratified mixtures under variable pressure and temperature conditions. Full details of the ECFM-LES formalism and of the transport equations for the filtered mass densities species $\overline{\rho}\widetilde{Y}_i$, the fuel tracer $\widetilde{Y}_{TF}$, the mean and fresh gases enthalpy can be found in [26, 28] and are therefore not given here. For the present calculations, only major species are considered: Fuel, O_2, N_2, CO_2, H_2O, CO and H_2. The composition of the burnt gases is obtained considering two reactions:

$$\begin{array}{c} \alpha[C_xH_y + (x+\frac{y}{4})O_2 \rightarrow xCO_2 + \frac{y}{2}H_2O] \\ (1-\alpha)[C_xH_y + \frac{x}{2}O_2 \rightarrow xCO + \frac{y}{2}H_2] \end{array} \quad (1)$$

The parameter α is defined following:

$$if \overline{\phi} < 1 : \alpha = 1 \text{ else } \alpha = \frac{\frac{4(x+\frac{y}{4})}{\overline{\phi}} - 2x}{2x+y} \quad (2)$$

where ϕ is the equivalence ratio. The species reaction rate $\overline{\dot{\omega}}_k$ and the heat release $\overline{\dot{\omega}}_{h_s}$ are then modeled following:

$$\overline{\dot{\omega}}_k = \overline{\rho}^u \widetilde{Y}_{TF} S_L \overline{\Sigma}_c \left(\alpha \nu_{k1}^{'} + (1-\alpha)\nu_{k2}^{'} \right) \quad (3)$$

$$\overline{\dot{\omega}}_{h_s} = \sum_k \Delta h_{f,k}^0 \overline{\omega_k} \quad (4)$$

$\nu_{k1}^{'}$ and $\nu_{k2}^{'}$ are the coefficients of reactions 1 and 2 of species k in Eq. (1). The burnt gas enthalpy is computed from the average and fresh gases enthalpy [26] following $\widetilde{h}_s^b = (\widetilde{h}_s - (1-\widetilde{c})\widetilde{h}_s^u)/\widetilde{c}$. The superscripts u and b refer to fresh and

burnt gases conditions, respectively. $\widetilde{c}$ is the Favre filtered progress variable defined using the fuel mass fraction according to $c = 1 - Y_{Fu}^{u}/Y_{TF}$. Y_{TF} is the fuel mass fraction before the onset of combustion [49]. The burnt gas temperature and density are therefore deduced knowing the composition and enthalpy of the burnt gases. The post-oxidation in the burnt gases is omitted in the present study as the fuel/air mixture is nearly homogeneous and lean or diluted.

Spark-ignition is modeled using the ISSIM-LES model [49] which includes the description of the electrical circuit and 3D modeling of the flame kernel growth during ignition. An electrical circuit model, based on the description provided by AKTIM [50, 51] defines the electrical power $P_{ign}(t)$ and energy $E_{ign}(t) = \int_{t_{spark}}^{t} P_{ign}(t')dt'$ transferred to the gas during the spark life (breakdown and glow phase), as well as the initial burnt gases profile and reaction rates. Throughout the ignition phase, the flame kernel evolution is directly controlled by the flame surface density equation, the source terms of which are modified during early ignition to accurately represent the flame surface growth. The burnt gas temperature is computed as described previously. ISSIM-LES thus accounts for the effect of mixture stratification, convection and turbulent stretch on the early flame kernel growth. As long as the flame radius r_b remains smaller than the combustion filter size $\hat{\Delta} = 5\Delta_x$ where Δ_x is the cell size and $\widetilde{c}$ is smaller than one, the flame kernel is described at the SGS level using ISSIM-LES. The burnt gases r_b is given by a transport equation to allow multi-sparks ignitions. When r_b approaches $\hat{\Delta}$, the progress variable $\widetilde{c}$ reaches unity and the transition between ISSIM-LES and ECFM-LES is progressively reached using a coefficient $\alpha = 0.5(1 + tanh(r_b/\hat{\Delta}) - 0.75/0.15)$ which is one during ignition and zero afterwards. This enables a smooth transition to the freely propagating turbulent flame. The impact of this criteria has not been examined here but it should be weak in this situation where the mesh size is small (0.2mm) so that transition occurs fast (a few degrees after spark-ignition).

The parameters of ISSIM-LES are set to reproduce the spark-ignition system used in the SGEmac experiments. It consists of a coil ignition system (Sagem type BAE 04). The spark gap is 1.2 mm, the total energy stored in the coil is

sufficiently high (about 600 mJ) to prevent misfires. The secondary inductance is around 30 H and the secondary resistance around 10 kΩ. The spark duration can vary from cycle to cycle as it depends on the available energy in the secondary spark and on the energy transferred to the gas, the evolution of which is given by an ODE and incorporates the time evolution of the spark length with the convection [51]. Overall, the spark life varies here between 500 and 600 μs, that is around 4 CAD.

In Eq. (3), the local laminar flame speed S_L is obtained from a correlation of Metghalchi and Keck [52, 24] as a function of local thermodynamic conditions, and with a correction to account for the dilution rate [48]. It takes the following form:

$$\overline{S}_L = \overline{S}_L^0 \left(\frac{\widetilde{T}^u}{T_0} \right)^{\alpha} \left(\frac{\overline{p}}{p_0} \right)^{\beta} (1 - 2.1\widetilde{X}_{dil}) \tag{5}$$

with $\alpha = 2.18 - 0.8(\widetilde{\phi} - 1)$, $\beta = -0.16 + 0.22(\widetilde{\phi} - 1)$, $T_0 = 298$ K, $p_0 = 1$ bar. In the ECFM-LES and ISSIM-LES approaches fuel chemistry is not explicitly solved for when determining the heat released by the flame, but is rendered implicitly via the laminar flame speed and its effect on spark-ignition, flame surface creation and destruction, and heat release rate.

3.5. Computing time

The computation of a full engine cycle of 720 CAD took about 55 hours on a number of cores between 256 and 512 of a SGI Altix ICE 8200. The number of cores was adapted to the varying mesh size during the different mesh phases in order to optimise the exploitation of parallelism during the full engine cycle.

4. LES of the stable operating point stab_ref

In order to validate the developed LES methodology, it was first applied to the simulation of twelve consecutive full engine cycles of the stable reference operating point stab_ref. The first two cycles were discarded (as they were in all other presented LES), as they are considered being polluted by the initial

conditions and the results were compared with experimental findings obtained by acquiring 100 consecutive cycles.

The ability of the present methodology to predict the intake flow observed experimentally has already been reported in [35] and will not again be detailed here.

Fig. 2 illustrates a typical flame propagation based on an individual LES realisation of stab_ref at four different instants after spark-ignition (SI). At $SI + 5\ CAD$, the flame is not spherical anymore, and exhibits a preferential propagation towards the exhaust side (negative x) under the effect of the mean flow velocity at the spark resulting from the tumble flow created during the intake stroke. Although it interacts earlier with the cylinder head on the exhaust side, it nevertheless keeps propagating at later instants faster towards the exhaust than towards the intake side, resulting in an overall elliptical shape. A similar behaviour was reported in the LES by Granet et al. [24] using the TFLES combustion model.

In order to assess the quality of the LES in terms of combustion, Fig. 3 shows the time evolution of the phase averaged ratio between the resolved flame surface $S_{res} = \int_V |\nabla \overline{c}| dV$ and the total flame surface $S_{tot} = \int_V \overline{\Sigma}_c dV$ as defined in [53], where $\overline{c}$ is the mass-weighted filtered progress variable such as $\overline{\rho}\widetilde{c} = \overline{\rho c}$. A ratio S_{res}/S_{tot} close to 0 indicates a RANS-type simulation, where the flame-turbulence interaction is entirely modeled, while a ratio close to 1 would correspond to a DNS. For the stab_ref case, the spatial resolution of the mesh during the first 20 CAD is sufficiently high to resolve around 80 % of the flame surface. In later stages, the spatial resolution becomes lower due to the mesh movement, yet still around 50 % of the flame surface is resolved. The same resolution is obtained in the two unstable cases as shown with the unst_lean case.

Fig. 4 compares the crank angle evaluations of the cylinder pressure predicted by the 10 LES cycles with experimental findings resulting from 100 engine cycles. Fig. 4(a) first superimposes the individual cycles predicted by LES on the experimentally acquired data. Despite the limited number of simulated

cycles, LES qualitatively yields a level of variability comparable to the experimental observations. The statistical comparison shown in Fig. 4(b) allows a more quantitative comparison. LES provides a very accurate reproduction of the experimental phase-averaged mean cylinder pressure evolution, but underestimates the level of cyclic variability. The latter is materialised via the statistical variation envelope computed from the LES and experimental individual cycles as:

$$\hat{p}_{cyl}(CAD) - 2\sigma(CAD) < \hat{p}_{cyl}(CAD) < \hat{p}_{cyl}(CAD) + 2\sigma(CAD), \qquad (6)$$

where $\hat{p}_{cyl}$ is the phase averaged cylinder pressure at a given crank angle CAD (normalised for all cycles between 0 and 720), and σ the standard deviation at a given crank angle resulting from a statistical phase averaged analysis of all individual engine cycles. For the sake of clarity, the symbol $\hat{}$ will be omitted thereafter.

Table 3 summarises the cycle averaged mean values and the variability of different variables resulting from a statistical analysis of the experiments and the present LES.

The variability is evaluated via a coefficient of variation (COV), defined as the standard deviation of the considered quantity X divided by the mean value, and expressed in %. It is computed for any quantity X as :

$$cov(X) = \frac{\sqrt{\frac{1}{N}\sum_{i=1}^{N}\left(X - \sum_{i=1}^{N} X/N\right)^2}}{\sum_{i=1}^{N} X/N}. \qquad (7)$$

where N is the number of realisations.

The IMEP is the cylinder pressure integrated as a function of the cylinder volume and it is used as a measure of indicated work output per cycle of a cylinder:

$$IMEP = \frac{1}{V_d}\int p_{cyl} dV, \qquad (8)$$

where V_d is the cylinder displacement volume. Table 3 confirms that the LES accurately reproduces the experimentaly observed mean trapped mass, IMEP and maximum cylinder pressure.

Comparisons of the COV of these quantities confirm that the CCV levels are under-predicted by our LES, by 18 % for the IMEP and up to 50 % for the trapped mass. Considering that the trapped mass is not a direct experimental observation, but results from an a posteriori analysis of individual experimental cycles that introduces additional uncertainty, and that its variability is very small, the present results can be considered as overall validating the ability of the proposed LES methodology to predict combustion in the SGEmac engine under stable operating conditions. Note that a very similar level of reproduction of experimental findings for the stable operating point were reported in [24], based on analysing 25 LES cycles.

5. LES of the unstable operating points

The developed LES methodology was applied to the study of combustion and its variability in the two unstable cases of the SGEmac database: unstab_dil, resulting from the above reference operating point by an important dilution of the fresh gases by N_2 (mimicking an increase in the external EGR rate), and unstab_lean, obtained from the reference point by a strong reduction of the overall fuel/air equivalence ratio.

These modifications of the fresh gases' composition have a strong effect on the laminar flame speed. Fig. 5 shows time evolutions of the statistical mean laminar flame speed averaged over the flame surface as a function of the crank angle. This information was extracted from the LES discussed in detail hereafter following:

$$< S_L >_s = \frac{\int S_L(x_i,t)\Sigma(x_i,t)dV}{\int \Sigma(x_i,t)dV} \tag{9}$$

where dV is the volume of the computational cell. As compared to the reference case, its value is strongly decreased for the unstable cases. Furthermore, its values for unstab_dil are 10 to 30 % smaller than those encountered for the

unstab_lean case during the ignition and propagation phases. An opposite trend is apparent in the late phases of combustion. These strong reductions of the laminar burning characteristics (laminar flame speed, but also the laminar flame thickness not shown here) do strongly modify the response of the flame to the turbulent in-cylinder flow during the ignition and combustion phases, and are the key factor for increasing the CCV as compared to the reference case.

5.1. Illustration of the combustion variability

Figs. 6 and 7 illustrate the cyclic variability predicted by the present LES for the unstab_dil and unstab_lean cases respectively. Top views of the combustion chamber are shown for 6 consecutive cycles taken at 35 CAD after spark-ignition, the flame being materialised by an iso-surface of the reaction rate coloured by the flow velocity. The time evolutions of the cylinder pressure of these cycles are also shown to distinguish slow burning cycles, leading to low cylinder pressure levels, from fast burning cycles exhibiting higher cylinder pressures.

Overall, the combustion proceeds in a qualitatively similar way to that observed for the stable reference case, with a generally faster propagation towards the exhaust side (negative x direction) as a result of the tumbling flow. However, an important level of variability is apparent for the two unstable cases, and important differences can be observed between slow and fast cycles. For the unstab_dil case, this is especially apparent when comparing cycle 17, the slowest of the shown cycles, and cycle 22 which is the fastest. The flame shape for the former is very elongated towards the negative x direction and has hardly propagated in the y direction, while the shape for the faster cycle is more isotropic, despite a preferential propagation towards the exhaust side. At the shown instant, the flame of cycle 22 occupies around 25 % of the chamber volume, while this value only reaches around 12 % for the slowest cycle 17. Fig. 7 exhibits a similar difference between the slowest shown cycle 15 of unstab_lean, occupying a small volume of the chamber and being very elongated towards the exhaust side, and the fastest cycle 16 that exhibits a more isotropic shape. A similar behaviour was reported in [24], and shown to result from interactions of the

early flame kernel with the spark plug cavity and from characteristics of the mean flow field. A detailed analysis will be presented below.

5.2. Reproduction of the experimental CCV

In order to quantify the CCV of the two unstable cases, 30 consecutive full engine cycles were simulated for both cases, using the developed methodology. The first two cycles of each case are discarded and the results are compared with experimental findings obtained by acquiring 200 consecutive cycles.

Figs. 8 and 9 compare LES results with experimental findings in terms of cylinder pressure and of FMBe. The latter stands for fuel mass fraction burnt (energetic) and is obtained from a combustion analysis, performed using an in-house analysis tool. This tool performs an instantaneous energy balance, during the combustion phase, based on the cylinder pressure trace, piston law, thermodynamic state of the trapped mixture, and on the wall heat losses estimated using a Woschni correlation [54]. The resulting overall instantaneous heat release rate is non-dimensionalized with the energy content of the trapped fuel mass, and integrated over time to yield the cumulative heat released that allows tracing overall combustion progress as well as its timing and duration. Both the experimental and simulated pressure traces were analyzed using this analysis tool.

Fig. 8 (a) superimposes cylinder pressure traces for individual LES cycles for the unstab_dil case and an experimental probability density function (PDF) resulting from the observed probability of reaching a specific cylinder pressure at a given crank angle. Fig. 8 (c) shows the corresponding FMBe curves and experimental PDF. Qualitatively, the cycles predicted by LES seem to reproduce the high cyclic variability observed in the experiments. However it is also apparent that the LES has a tendency to predict overall slower cycles than in the experiments, no LES cycle corresponding to the fastest experimental cycles, and one LES cycle being slower than statistically observed. A quantitative analysis is proposed in Fig. 8 which compares the mean and statistical envelope of cylinder pressure predicted by LES with experiments. The evolution of the average

cylinder pressure and overall combustion progress are very well retrieved by the LES, with a slight under-prediction of the statistical occurrence of the slowest and fastest cycles by our LES. This is confirmed by the corresponding FMBe evolutions shown in Fig. 8 (d) up to a crank angle of 40 CAD. At later instants, major differences become apparent in terms of FMBe between LES and experiments. However, combustion analysis is typically known to be prone to high errors during the late combustion phase, when the flame is close to the chamber walls. The FMBe prediction should therefore not be interpreted quantitatively in the late combustion stages, due to important errors in predicting wall heat losses for the analysis. Therefore, the incomplete combustion predicted by the combustion analysis is certainly highly over-estimated, but it should nevertheless be underlined that for few extreme LES cycles combustion was uncomplete at EVO (see below). The observed discrepancy in terms of FMBe could possibly indicate modeling shortcomings, of either the turbulent combustion model, or the wall heat loss model. In the absence of sufficiently detailed experimental evidence on the late combustion stages, this was not further explored.

Fig. 9 presents the corresponding findings for the unstab_lean case. The spread of individual cylinder pressures and FMBe is very well reproduced by the LES, and appears qualitatively better centred within the experimentally observed envelope than for the unstab_dil case. This is confirmed looking at the statistical analysis shown in Figs. 9 (b) and (d), the mean cylinder pressure and combustion progress as well as the upper limit of their variability envelope being statistically accurately retrieved. However, the lower limit of the variability envelope for the cylinder pressure is not exactly reproduced by the LES, but appears satisfactory. The reproduction of the mean time evolution of the FMBe and of its variability envelope are very satisfactory, even in late combustion stages. Finally, the slowest cycles did also lead to an incomplete combustion until EVO.

Fig. 10 compares the Matekunas diagrams predicted by LES with experimental findings for the stable and the two unstable operating points. In this diagram, the maximum cylinder pressure of each cycle is plotted against the

crank angle of its occurrence. The experimental results are colored by their probability of reaching their instantaneous values. Matekunas identifies 3 zones: a linear zone where p_{max} and CA(p_{max}) vary linearly, a hook-back area where p_{max} varies much more than CA(p_{max}) and a return zone with only small variations of p_{max}. The cycles of the stable case are always located in the linear zone, while clear departures can be observed for the unstable cases. The LES results reproduce quite well the experimental findings, although the LES of the lean case appears to predict slightly earlier CA(p_{max}) than found in the experiments. More quantitative comparisons are provided in the following Section.

5.3. Quantitative validation of the CCV predictions

The combustion process is usually divided in four main stages [1]. First, the sparking and flame initiation correspond to the formation of a flame kernel during the spark life (the first 500 μs in the present situation), which can be successful or not, depending on the energy deposit and flow conditions in the vicinity of the spark. In our case, the flame kernel initiation is always successful. Then the initial flame kernel development is defined as the period during which the burnt gas mass fraction reaches 1 to 2 %. It ends when the flame kernel reaches a size at which it is influenced by large eddies. These two stages correspond here to the ignition phase. The third phase is the turbulent propagation, followed by the last phase that corresponds to the end of combustion when the flame extinguishes at the combustion chamber wall.

In order to yield a more quantitative assessment of the quality of reproduction of the experimentally observed CCV by the present LES, Table 4 details the cycle averaged mean and variability of different parameters characterizing the two unstable cases, The $CA2$ and $CA50$ values are defined as the crank angle at which the FMBe reaches respectively 2 % and 50 %. The $CA2$ is representative of the ignition phase while $CA50$ corresponds to the fully turbulent propagation.

Overall, the more accurate reproduction of experimental findings is obtained for the lean case: the mean trapped mass, IMEP and maximum cylinder pressure

are reproduced within a 6 % error margin. The differences between LES and experiments in this case are related to a slightly too high overall combustion speed predicted by the simulations. LES predicts a mean $CA2$ which is 1.2 CAD in advance of the experiments, and up to 2.6 CAD in advance for the mean $CA50$. The level of variability predicted by the LES is generally satisfactory: the COV of the maximum cylinder pressure is slightly under-estimated, while the COV of $CA2$ and $CA50$ are rather over-estimated. A major discrepancy appears for the COV of trapped mass. The reason for this deviation could not be identified, but one can note that in any case the experimental COV of trapped mass is small (0.3 %), so that it is not a major source of CCV.

For the diluted case, the mean and variability of the trapped mass are very accurately reproduced by the LES. The error of prediction of mean IMEP and maximum pressure are of the same order than for the lean case. This also holds for the mean $CA2$, the combustion progress being predicted slightly in advance, while the $CA50$ is quite well retrieved. In terms of variability, the COV levels of all parameters are slightly over-estimated by LES, yet satisfactory. The highest discrepancy in terms of COV is found for IMEP, where the LES over-estimates the experimental value by 20 %.

6. Analysis and quantification of CCV sources

6.1. Comparison of slow and fast cycles

In order to compare slow and fast cycles of the two unstable cases, the flame propagation is visualised for different CA degrees after the spark ignition using the same iso-surface as in Section 4 and vertical central cuts showing the reaction rate. The two cycles that are systematically compared are characterized by very different combustion speeds, but have similar trapped masses and gas composition.

Fig. 11 left, compares results for the fast (C9) and the slow cycle (C17) predicted by the LES of the diluted case. During the early ignition the flame is first driven into the spark plug cavity for both cycles, and both exhibit a similar

initial flame kernel growth rate. Later, at 35 CAD after ignition, the flame of cycle 9 however propagates faster into the rest of the chamber than for cycle 17. These differences coincide with the evolution of the flow velocity in the flame vicinity. The latter is characterized by spatially averaging the fresh gas velocity components along the flame front as:

$$< \widetilde{u}(t)|_{\widetilde{c}=0.001} >= \frac{\int \widetilde{u}(x_i,t)|_{\widetilde{c}=0.001} dV}{\int \delta(\widetilde{c}-0.001) dV} \tag{10}$$

Fig. 11 right, shows the crank angle evolution of these axial (top) and vertical (bottom) fresh gases velocities. During early ignition, the axial velocity of cycle 17 is small compared to that for cycle 9, and there is a quite strong positive (i.e. upward) vertical component. This combination tends to counteract the propagation of the flame out of the spark cavity. In opposition, cycle 9 exhibits a clearly higher (and negative) axial fresh gases velocity, combined with a smaller and even negative vertical component, which both favour the propagation downward and away from the spark plug. The sudden increase of the axial velocity (in amplitude) that occurs 20 to 30 CAD after ignition for both cases coincides with the flame propagation outside the cavity in regions with higher velocities.

Fig. 12 proposes a comparable analysis for the lean case. In the slower cycle 21, the flame kernel can hardly propagate out of the spark plug cavity as clearly seen at 17 CA degrees after spark timing. Later, the flame is cut in two, but the flame propagating out of the cavity is small and a fraction is quenched at the walls. On the contrary, in cycle 18, the flame can propagate outside the spark plug cavity from the very beginning of the ignition, and grows much faster into the main part of the chamber. The comparisons of the fresh gas velocity components initially show similar axial velocities at ignition timing, but later on the vertical velocity for cycle 21 is positive and large thus counteracting the flame propagation away from the spark. On the contrary, the high negative vertical fresh gases velocity for cycle 18 greatly facilitates the propagation away from the spark plug. For both cases, the fresh gas velocity seen by the flame approaches zero when the flame front reaches the wall.

Fig. 13 presents plots of the CA2 versus CA50 for the LES and experiments

of the stable and the two unstable cases. These curves show that on average, the smaller the CA2 (i.e. the faster the initial burning phase), the smaller the CA50 (the faster the main combustion phase). The standard deviation of the scatter plots is close to 1 degree in the stable case, 1.25 degree in the lean one and 2 degrees in the diluted case. The LES reproduce the overall experimental tendencies. It is interesting to note that some extreme cycles contradict the average correlation, both in LES and experiments, which will be studied below.

This first analysis of the CCV in the unstab_dil and unstab_lean cases reveal that the flame is strongly perturbed by the flow motion in particular during the early combustion phase, that in turn impacts the ensuing flame development and overal combustion duration.

6.2. CCV sources and correlations

The above presented analysis allows studying 3D phenomena as the local interactions of the flame with the flow and chamber geometry, but it does not help identifying overall dependencies. In order to achieve the latter in what follows, quantities describing the combustion efficiency and speed are correlated with local and global parameters in order to attempt identifying statistical correlations.

Thereafter all local quantities are spatial averages over a radius of 1 mm at the spark plug center at ignition timing, and are identified with the subscript $_{spk}$. To quantify the correlation, Bravais-Peason correlation coefficients are used:

$$R = \frac{\sigma_{xy}}{\sigma_x \sigma_y} \tag{11}$$

where σ_{xy} is the covariance of variables x and y, and σ_x and σ_y are their standard deviations. A value of $|R|$ close to 1 implies that x and y are perfectly linearly correlated. A value of 0 indicates that there is no correlation. The sign of R indicates the sign of the slope of the regression line.

The spark energy as a source of cyclic combustion variability is discarded since a very high amount of energy is deposited after each breakdown to pre-

vent misfires or ignition delays. Preliminary experimental and numerical tests performed in the two unstable cases confirmed that variations of the energy transferred to the gas and of the spark life duration has negligible impact on the combustion process.

In the diluted case, the fraction of fuel and air is held constant for all cycles. As the mixture is stoichiometric, an incomplete combustion leads to the same proportion of unburnt fuel and air, but to a different amount of unburnt fuel mass. The in-cylinder fuel mass of cycle n is therefore partially correlated between subsequent cycles as shown in Fig. 14. In the lean case, there is no correlation between subsequent cycles.

In order to quantify the impact of thermodynamic variability on the ignition process, correlation coefficients between different local and global variables and the local laminar flame speed at ignition timing were computed. The explored variables were : temperature, equivalence ratio, fraction of dilution gases Y_{dil}, dilutation rate τ_{dil} and residual gas rate τ_{res}. The three latter quantities were computed as described hereafter. The combustion chamber contains a total trapped mass (m_{tot}) which is the sum of the residual gas mass (m_{res}) and of the mass of air and fuel induced during the intake stroke. The residual gases are composed of variable proportions of fresh and burnt gases left over from the previous cycle. The trapped mass m_{tot} can also be defined as the sum of the fresh gases (fuel + air) and of dilutant (m_{dil}):

$$m_{dil} = m_{CO} + m_{CO_2} + m_{H_2} + m_{H_2O} + m_{N_2} - \frac{3.76 W_{N_2} Y_{O_2}}{W_{O_2}} m_{tot}, \qquad (12)$$

where Y_{O_2} is the oxygen mass fraction, W_{N_2} and W_{O_2} the molecular masses of nitrogen and oxygen. The last RHS term of Eq. (12) is the mass of N_2 coming from the fresh air introduced in the combustion chamber during intake. The mass m_{N_2} in Eq. (12) includes the mass of N_2 dilutant introduced during intake in the diluted case. The dilution and the residual masses are normalized by the trapped mass to yield respectively the dilution rate ($\tau_{dil} = m_{dil}/m_{tot}$) and the residual rate ($\tau_{res} = m_{res}/m_{tot}$).

The local fraction of dilutant Y_{dil} is defined:

$$Y_{dil} = Y_{CO} + Y_{CO_2} + Y_{H_2} + Y_{H_2O} + Y_{N_2} - \frac{3.76 W_{N_2} Y_{O_2}}{W_{O_2}}, \tag{13}$$

The mean in-cylinder temperature is not deeply analysed since its variation is negligible (about 2K) since it is related to the quasi-constant values of the in-cylinder total mass and pressure at spark timing. As a result, the variations of the dilution rate and of the trapped fuel mass are perfectly correlated, as shown in Figs. 15. Tables 5 and 6 summarize the different correlations between the aforementioned quantities for the two unstable cases. The highest correlations are written in red, the lowest values appear in yellow and intermediate ones in orange. The mean and standard deviations (in percent) of each variable is also provided in the first row. For the diluted point, S_L is strongly correlated with the local and global dilution gas fraction, which are also highly correlated with each other. Indeed, the additional dilutant (N_2) is perfectly premixed with the fresh intake gases. During intake and compression strokes it mixes with the residual gases so that at spark ignition timing, the mixture is almost homogeneous. A moderate correlation is found between S_L and the temperature with a negative value, the temperature being partially correlated with the dilution rate. This result seems in contradiction with the fact that the laminar flame speed depends on the square of fresh gases temperature (using Eq. (5)). Furthermore, the analysis of Pera et al. [55] shows that the effect of temperature heterogeneity is dominant over the dilution effect. An explanation can be found when examining Fig. 16 showing the evolution of the computed laminar flame speed as a function of the temperature and of the dilution rate within the range of values encountered at ignition timing. The maximum variation of the laminar flame speed reaches 26 % of the mean value over the range of variation of the dilution rate, while it reaches only 7 % with the temperature. Therefore, the impact of the dilution is stronger than the one of the temperature in these conditions. The local fluctuation of temperature is generated by both the wall heat transfer and the mixing with hot residual gases, while the variation of the local dilution rate composed of N_2 dilutant from the intake (initially cold) and

hot burnt gases from the previous cycle is rather related to the variation of the global composition. Consequently, an increase of the dilution gas fraction is followed by a decrease of the flame speed. We may conclude that in this case, the combustion progress is rather influenced by the variation of global quantities (the amount of available fuel mass is perfectly correlated with the burnt gas mass) than that of the local temperature. For the lean case, Table 6 shows high correlations between the laminar flame speed and temperature, dilution gas fraction and the local and global equivalence ratio, which are also well correlated to each other. For this case, the burnt gas rate is weak (5 %), so that an increase of the temperature or of the burnt gas fraction leads respectively to an increase and a decrease of the laminar flame speed. The increase of the temperature is also well correlated with the increase of the residual gas rate composed of burnt gases and excess air.

Correlations with different local and global quantities describing the flow motion were then examined. Fig. 17 (a) and (b) correlates the tumble number as a function of the average resolved kinetic energy in the cylinder. The tumble number $T_y = H/(M\omega_{eng})$ is defined using the momentum H, the moment of inertia M and the engine speed ω_{eng} in rad/s. Here these quantities are extracted at spark timing. For the two unstable cases, both quantities are clearly correlated (0.71 in the diluted case and 0.61 in the lean case) : the higher the magnitude of T_y, the higher the global level of kinetic energy. This result confirms that the tumble motion is a key flow feature. The tumble numbers and the kinetic energies are of the same order of magnitude for the two studied operating points.

Fig. 17 (c) to (f) correlates the resolved velocity magnitude and the axial resolved velocity u in the vicinity of the spark at ignition timing with the tumble number. Surprisingly, no correlation is found between the local velocity amplitude and the tumble number. u and T_y are only partially correlated in the lean case ($R = 0.43$), while no correlation is found in the diluted case. However we notice that the slowest cycle (C15) of the unstab_lean case is characterized by both very low local velocity at spark and tumble number. As seen in Sec-

tion 6.1 strong variations of the local velocity are observed in the vicinity of the spark. These variations are related to the local flow motion (vortices, turbulence) rather than directly to the tumble motion.

The effect of the cycle-to-cycle dependency of combustion on thermodynamic and aerodynamic parameters was then investigated by studying their correlations with IMEP. First of all, single linear regression models were used. Fig. 18 presents the resulting histogram of the correlation coefficients between IMEP and different variables X_i for the two unstable cases. Similar patterns filling the bars indicate variables which are correlated to each other. The correlations with IMEP of the following variables were examined (in the order of appearance in Fig. 18):

- $(\widetilde{w}/\widetilde{u})_{spk}$, the ratio between the resolved vertical and axial velocity components
- $\widetilde{\phi}_{spk}^{inhom}$, a measure of the resolved equivalence ratio inhomogeneity defined in Eq. (14)
- $\widetilde{\phi}$, the mean in-cylinder equivalence ratio
- m_{fu}, the in-cylinder unburnt fuel mass after the end of intake
- $\widetilde{Y}_{dil,spk}$, the resolved mass fraction of dilutant defined in Eq. (13)
- m_{air}, the in-cylinder air mass
- τ_{dil}, the dilution rate defined using Eq. (12)
- $|\widetilde{U}|_{spk}$, the resolved norm of velocity
- E_{T_y}, the tumble energy defined in Eq. (16)
- $IMEP^{n+1}$, IMEP of the subsequent cycle
- E_c, the resolved kinetic energy
- m_{tot}, the total in-cylinder mass

- u_{spk}^{sgs}, the subgrid scale velocity (at the combustion filter size)
- τ_{res}, the residual rate
- $\widetilde{T}_{spk}^{inhom}$, a measure of the resolved temperature inhomogeneity defined in Eq. (15)

The local equivalence ratio and temperature inhomogeneities in the spark plug vicinity $\widetilde{\Phi}_{spk,inhom}$ and $\widetilde{T}_{spk,inhom}$ were evaluated following a monoparametric regression study as:

$$\widetilde{\Phi}_{spkp}^{inhom} = \widetilde{\Phi}_{spk} - a\widetilde{\Phi}, \quad a = 1.0785 \tag{14}$$

$$\widetilde{T}_{spk}^{inhom} = \widetilde{T}_{spk} - a'\widetilde{T}, \tag{15}$$

where $a' = 1.6177$ for unstab_lean and $a' = 3.3645$ for unstab_dil were found.

The tumble energy E_{T_y} was determined following:

$$E_{Ty}(CA) = m_{tot}\left[T_y \omega_{eng} D(ST)/4\right]^2, \tag{16}$$

D is the distance between the piston and the top of the cylinder head and ST is the crank angle of spark timing.

In Fig. 18, lines corresponding to a coefficient of correlation $|R| = 0.4$ are plotted to indicate approximately the level above which correlations are significant. For the diluted case, Fig. 18(a) indicates that the thermodynamic quantities have the most important effect on the IMEP in terms of cyclic variations and that they are all correlated with each other. Aerodynamic quantitites characterizing the large scale turbulence (tumble energy E_{T_y} and kinetic energy E_c) and the local resolved and subgrid scale velocity ($|\widetilde{U}|_{spkplg}$ and u_{spkplg}^{sgs}) together seem to have a second order but still significant impact. It is noteworthy that $|\widetilde{U}|_{spkplg}$ is well correlated with the axial velocity $\widetilde{u}$ which is generated by the tumble motion.The correlation of the IMEP with the subsequent cycle $IMEP^{n+1}$ is weak. Other quantities are negligible : the total enclosed mass which varies only weakly, the residual gas rate and the local flow direction, described by the ratio between the vertical velocity $\widetilde{w}$ and the axial velocity $\widetilde{u}$.

On the contrary, for the lean case, Fig. 18(b) shows that the main source of the IMEP variability is clearly the ratio $\widetilde{w}/\widetilde{u}$ with a coefficient of correlation $|R| = 0.86$. Then thermodynamic variations influence partially the combustion variability. For both cases similar correlations are found between the IMEP and the enclosed fuel mass (0.54) and the dilution gas rate (0.49).

6.3. Multidimensional data analysis

The previous analysis has highlighted the relationships between combustion characteristics and flow/thermodynamic parameters. However the single regression analysis reaches a limit when several parameters act simultaneously, as it is the case in the present results, making it difficult to identify the most important factors and to obtain relevant correlation coefficients. In order to achieve a more relevant overall picture of the most important parameter impacting CCV, a multivariate regression model was used. In the proposed approach, a relationship between the dependent response $IMEP(n)$, where n is the cycle number, and different independent parameters or variables $X_i(n)$ is explicitely estimated. As the type of regression (linear, gaussian, polynomial...) between the variables is unknown, and as in the present cases the standard deviation of any variable did never exceed 8 %, we assumed here a linear multiple regression.
To this purpose,the following steps were followed:

1. First the necessary condition for selecting the X_i among all the possible parameters is that the X_i vectors are non collinear, and that $n > p + 1$, where p is the number of variables. These variables may be defined based on a correlation analysis between every all available variables X_i in order to determine whether quantites are collinear or not. This step could also have been carried out using Principal Component Analysis [56]: it is a mathematical tool to reduce data space dimensions and compute linear combinations of the initial variables that are called principal components and which are uncorrelated to each other. However this method is beyond the scope of the present study as we need to manipulate physical quantities, and not complex linear combinations between them.

2. The matrix equation system $IMEP(n) = \sum_{i=1}^{p} \beta_i X_i(n) + \epsilon(n)$ is solved using a least-squares fit which provides the constant slopes β_i and the residuals $\epsilon(n)$ of the equation. The $X_i(n)$ are normalised by their mean value to avoid that any variable has a larger impact due to its scale.
3. The degree of correlation between X_i and the response $IMEP$ is examined by calculating the coefficient of correlation between X_i and $IMEP - \sum_{k \neq i}^{p} \beta_k X_k$, thus discarding the contribution of the other variables.
4. The degree of correlation between $IMEP$ and the resulting model $\sum_i \beta_i X_i(n) + \epsilon(n)$ is examined. A correlation coefficient R greater than 0.7 is usually considered as strong correlation.
5. If the contribution of variable X_i is not significant in the resulting model (typically $|R_{XY}| < 0.4$), then it is suppressed from the equation and step (2) is repeated. If several sets of variables can be identified, steps (1) to (3) are performed with each of them to find the most relevant one, providing the final, best fitting model.

Following steps (1) to (5), the following set of independent variables was identified :

- For the unstab_dil case: m_{fu}, $|\widetilde{U}|_{spk}$, u^{sgs}_{spk}, E_{T_y} and $\widetilde{T}^{inhom}_{spk}$.
- For the unstab_lean case: m_{fu}, $|\widetilde{U}|_{spk}$, $(\widetilde{w}/\widetilde{u})_{spk}$, $\widetilde{T}^{inhom}_{spk}$, $\widetilde{\phi}^{inhom}_{spk}$.

The modeled cylinder pressures are finally obtained as : $IMEP^{model}(n) = \sum_{i=1,5} \beta_i \widetilde{X}_i(n) + \epsilon_i$ with $\widetilde{X}_i = (m_{fu}, |\widetilde{U}|_{spk}, u^{sgs}_{spk}, E_{T_y}, \widetilde{T}^{inhom}_{spk})$ in the diluted case and $\widetilde{X}_i = ((\widetilde{w}/\widetilde{u})_{spk}, |\widetilde{U}|_{spk}, m_{fu}, \widetilde{\phi}^{inhom}_{spk}, \widetilde{T}^{inhom}_{spk})$ in the lean case. The obtained best fitting models for the two unstable cases are shown in Figs. 19 and 20 respectively for the diluted and lean cases. The first bar on the left in addition gives the correlation coefficient between IMEP and the obtained best fitting model IMEP^{model}, thus measuring the achieved degree of approximation by the multivariate model. The correlation coefficient between IMEP and its models is 0.93 for unstab_lean, indicating a high accuracy. For the unstab_dil case it is 0.8, showing a still sufficient yet slightly less accurate reproduction

of the observations. A reason for this discrepancy is probably that the flame is more strongly perturbed by the turbulent flow during the whole combustion phase, so that the diluted case could require taking into account other relevant physical parameters to improve the model accuracy. This was not attempted in the present study.

Two correlation coefficients between IMEP and the identified variables $\widetilde{X}_k$ are shown in Figs. 19 and 20:

- The left bars filled with dots indicate correlation coefficients obtained between the $\widetilde{X}_k$ and IMEP via the single regression model;
- The right bars filled with lines indicate the correlation coefficients from the multivariate analysis between the independent variables $\widetilde{X}_k$ and $IMEP - \sum_{i \neq k} \beta_i \widetilde{X}_i(n)$, i.e. discarding the contributions of the other idependent variables.

For most variables, the correlation obtained from the analysis confirms the findings from single regression, but the level of correlation is generally higher. The noticeable exception is the correlation for temperature inhomogeneities at the spark plug : the multivariate correlation is much higher for unstab_lean than for the single regression, the opposite trend appearing for unstab_dil. Overall this parameter is found negligible for both cases in the multivariate analysis. In summary and to first order, the multivariate analysis indicates that for the diluted case, the main parameters correlated with IMEP variablity are in-cylinder fuel mass, local resolved and subgrid-scale velocity at spark and the tumble energy. In the lean case, IMEP variability is mainly correlated to variations of local resolved velocity components and amplitude, and to the in-cylinder fuel mass. Temperature inhomogeneities at the spark plug do have a weak impact.

6.4. Qualitative classification of CCV

Finally, we compared our qualitative findings concerning the relative importance of different sources of CCV for the lean and diluted cases of the studied

engine with the ones identified by Ozdor et al. [1]. They reviewed different indicators of CCV from a substantial number of experimental studies. They involved two and four stroke, single and four cylinder SI engines, running on various fuels (iso-octane, propane, gasoline, toluene, methanol) either in premixed, carbureted or port fuel injection mode. Furthermore, different spark-ignition systems and spark plug locations, different dilution rates by nitrogen (0 to 15%), several equivalence ratios (lean and stoichiometric), different combustion chamber geometries, piston speeds, loads and swirl ratios were included. The result was a qualitative estimation of the phenomena influencing the CCV levels.

Following the results achieved in the present work, a similar classification could be obtained for the studied engine, but in our case based. The obtained results are summarized in Table 7, and compared with findings from Ozdor et al. [1], distinguinshing the impact on the spark-ignition and main combustion phase respectively.

Concerning spark-ignition, the convection in the spark plug region is the variable having the highest impact on CCV, which confirms findings by Ozdor et al. For the diluted case, its importance is comparatively smaller and of comparable importance to that of the global dilution rate. No other main factor was identified by our LES, in constrast to the lean case and to work by Ozdor et al. For the latter, comparable secondary levels of importance are found for the the global equivalence ratio and dilution rates, and to a lesser extend for spatial mixture inhomogeneities at the spark plug. Generally speaking, the classification proposed by Ozdor et al. is quite similar to the one obtained for the lean case, but exhibit some discrepancies with the diluted case.

The effect of composition variation affecting the laminar flame speed and therefore the beginning of the combustion is second order in the lean case through the equivalence ratio, the temperature and the burnt gas fraction and first order in the diluted case through the burnt gas fraction. During the whole

propagation, the variation of the intake energy (fuel mass) has a strong impact in both cases. The tumble motion has moderate effect in the diluted case while it is negligible in the lean case. Concerning the impact on the main combustion phase, the lean and diluted cases do not exhibit any single major factor having a higher relative impact than others on CCV. The present LES underestimates the relative importance of factors as in particular the overall fuel mass, mixture inhomogeneities and flow energy as compared to Ozdor et al.

Globally, the LES results confirm major findings by Ozdor et al., despite some important differences do appear. These differences should however not be over-interpreted, as Ozdor's findings were the result of a compilation of a wide range of engines and modes of operation, while the present LES concerned only two operating points of a single engine type.

7. Conclusion

This paper presents comparisons between Large-Eddy Simulations and experimental findings on cyclic combustion variability in a single cylinder spark-ignition engine fueled with a premixture of air and gaseous propane. Three operating points from the SGEmac database were studied : a stable reference operating point with low CCV levels, and two unstable points with high CCV, obtained from the reference case either by reducing the fuel/air equivalence ratio (lean case), or by adding an important external dilution by nitrogen (diluted case).

In the presented LES, spark-ignition was modeled using ISSIM-LES [49], which describes the electrical circuit of the spark and provides 3D modeling of the flame kernel growth during ignition, coupled to the ECFM-LES [28] turbulent combustion model which describes the flame front propagation.

A simulation methodology was employed that imposes in/outflow bound-

aries of the LES domain from system simulations of the complete engine set-up.

The proposed LES methodology based on the AVBP code was first shown to reproduce accurately the experimental findings for the stable reference operating point. It was then applied to perform multi-cycle LES comprising 30 full consecutive engine cycles for each of the two unstable cases. Detailed comparisons with experiments allowed validating the ability of the proposed methodology to accurately reproduce the phase-averaged mean and variability of in-cylinder pressure and combustion progress, as well as of other combustion characteristics and in particular IMEP.

The LES results were then post-processed with the aim of identifying causes for the observed CCV. A qualitative comparison between slow and fast burning cycles of the two operating points allowed illustrating how a combination of local velocity fields and geometrical features of the chamber as the spark plug cavity in the pentroof head concur to generate cyclic variability.
In order to yield a more quantitative estimation of the relative importance of different parameters on the occurrence of CCV, their individual impact was evaluated using single parameter regression models for their dependency on the cyclic varying IMEP. It was shown that despite the overall similarity between the diluted and lean operating point, the ensemble of most relevant parameters differ notably for the two cases. As the single regressions can hardly be used in a systematic approach to identify major causes of CCV, a multivariate regression was proposed and applied to both cases. It allowed identifying in a more systematic way the main parameters impacting IMEP variability. It also provided an explicit model linking the latter to first order to the variations of a limited set of independent, both local and global, parameters.

Finally a qualitative comparison of the relative importance of different local and global parameters as sources of CCV for the two studied cases was compared with findings from an extensive experimental survey of CCV sources by

Ozdor et al. [1]. Overall the latter findings could be confirmed by the presented analysis of LES, but also indicated that the detailed causes of CCV will probably depend on the type of engine and combustion mode.

This approach may bring objective elements to engineers for better understanding CCV sources on a given engine design or specific operating conditions. Such information is essential for improving design rules and is inaccessible to experiments. In this sense the proposed exploitation of LES is today unique and opens a large application field to this CFD tool in the piston engine industry. Future work will concern comparative studies for gasoline direct injection engines, in which the complex interactions between the fuel spray and intake aerodynamics will require specific LES studies and could potentially require more sophisticated regression models (quadratic or non linear).

8. Acknowledgements

This work was financially supported by the European Union under project N. 233615 LESSCCV of the 7^{th} framework programme for research (FP7).
The project was granted access to the HPC resources of CINES under allocation N. 026139 from the GENCI (Grand Equipement National de Calcul Intensif) eDARI program. We also thanks Abdelaziz Faraj and Frédéric Nicolas from IFPEN for valuable discussions on the multivariate analysis.

References

[1] N. Ozdor, M. Dulger, E.Sher, Cyclic variability in spark-ignition engines. a literature survey, SAE Paper 940987.

[2] J. Heywood, Internal combustion engine fundamentals, 2nd Edition, McGraw Hill, New York, 1988.

[3] W. Chen, D. Madison, P. Dice, J. Naber, B. Chen, S. Miers, M. Czekala, C. Glugla, Q. Qu, G. Huberts, Impact of ignition energy phasing and spark

gap on combustion in a homogenous direct injection gasoline si engine near the egr limit, SAE Paper 2013-01-1630.

[4] A. Robert, S. Richard, O. Colin, L. Martinez, L. D. Francqueville, Les prediction and analysis of knocking combustion in a spark ignition engine, Proc. Combust. Inst. 35 (3) (2015) 2941–2948.

[5] A. Robert, S. Richard, O. Colin, T. Poinsot, Les study of deflagration to detonation mechanisms in a downsized spark ignition engine, Combust. Flame 162 (7) (2015) 2788–2807.

[6] J. Rudloff, J.-M. Zaccardi, S. Richard, J. Anderlohr, Analysis of pre-ignition in highly charged si engines: Emphasis on the auto-ignition mode, Proc. Combust. Inst. 34 (2) (2011) 2959–2967.

[7] J.-M. Zaccardi, L. Duval, A. Pagot, Development of specific tools for analysis and quantification of pre-ignition in a boosted si engine, SAE Paper 2009-06-15.

[8] P. Adomeit, O. Lang, S. Pischinger, R. Aymanns, M. Graf, G. Stapf, Analysis of cyclic fluctuations of charge motion and mixture formation in a disi engine in stratified operation, SAE Paper 2007-01-1412.

[9] B. Thirouard, J. Cherel, Nature of cai combustion and air/fuel ratio stratification effects, Oil & Gas Sci. and Tech., Rev. IFP61 (1) (2006) 95–119.

[10] P. Adomeit, A. Sehr, R. Weinowski, K. Stapf, D. Seebach, S. Pischinger, K. Hoffmann, F. Abel, F. Fricke, H. Kleeberg, D. Tomazic, Operation strategies for controlled auto ignition gasoline engines, SAE Paper 2009-01-0300.

[11] J. Bedford, G. Brereton, H. Schock, R. Herrin, Measurements of cycle to cycle variability of the inlet flow of fuel injectors using lda, SAE Paper 2006-01-3314.

[12] H. Persson, R. Pfeiffer, A. Hultqvist, B. Johansson, H. Str´om, Cylinder-to-cylinder and cycle-to-cycle variations at hcci operation with trapped residuals, SAE Paper 2005-01-0130.

[13] P. Mehrani, H. Watson, Modeling the effects of mixture composition on cyclic variablity, SAE Paper 2007-01-0672.

[14] T. Poinsot, D. Veynante, Theoretical and Numerical Combustion, 2nd Edition, R.T. Edwards, 2005.

[15] P. Aleiferis, Y. Hardalupas, A. Taylor, K. Ishii, Y. Urata, Flame chemiluminescence studies of cyclic variations and a/f ratio of the reacting mixture in a si engine, Combust. Flame 136 (1-2) (2004) 72–90.

[16] P. Aleiferis, A. Taylor, J. Whitelaw, K. Ishii, Y. Urata, Cyclic variations of initial flame kernel growth in a honda vtec-e lean-burn spark-ignition engine, SAE paper 2000-01-1207.

[17] A. Banaeizadeh, A. Afshari, H. Schock, F. Jaberi, Large-eddy simulations of turbulent flows in internal combustion engines, Int. J. Heat Mass Transfer 60 (2012) 781–796.

[18] V. Huijnen, L. Somers, R. Baert, Study of turbulent flow structures of a practical-steady engine head flow using large-eddy simulations, J. Fluid Eng.-T ASME 128 (6) (2006) 1181–1191.

[19] I. Celik, I. Yavuz, A. Smirnov, J. Smith, E. Amin, A. Gel, Prediction of in-cylinder turbulence for ic engines, Combust. Sci. Tech. 153 (1) (2000) 339–368.

[20] D. Haworth, Large eddy simulation of in-cylinder flows, Oil & Gas Sci. and Tech., Rev. IFP54 (2) (1999) 175–185.

[21] R. Tatschl, M. Bogensperger, Z. Pavlovic, P. Priesching, H. Schuemie, Les simulation of flame propagation in a direct-injection si-engine to identify the causes of cycle-to-cycle combustion variations, SAE Paper 2013-01-1084.

[22] D. Goryntsev, A. Sadiki, J. Janicka, Analysis of misfire processes in realistic direct injection spark ignition engine using multi-cycle large eddy simulation, Proc. Combust. Inst. 34 (2) (2013) 2969–2976.

[23] M. Drake, D. Haworth, Advanced gasoline engine development using optical diagnostics and numerical modeling, Proc. Combust. Inst. 31 (2007) 99–124.

[24] V. Granet, O. Vermorel, C. Lacour, B. Enaux, V. Dugué, T. Poinsot, Large-eddy simulation and experimental study of cycle-to-cycle variations of stable and unstable operating points in a spark ignition engine, Combust. Flame 159 (4) (2012) 1562–1575.

[25] B. Enaux, V. Granet, O. Vermorel, C. Lacour, C. Pera, C. Angelberger, T. Poinsot, Les study of cycle-to-cycle variations in a spark ignition engine, Proc. Combust. Inst. 33 (2011) 3115–3122.

[26] O. Vermorel, S. Richard, O. Colin, C. Angelberger, A. Benkenida, D. Veynante, Towards the understanding of cyclic variability in a spark ignited engine using multi-cycle les, Combust. Flame 156 (2009) 1525–1541.

[27] O. Colin, F. Ducros, D. Veynante, T. Poinsot, A thickened flame model for large eddy simulations of turbulent premixed combustion, Phys. Fluids 12 (7) (2000) 1843–1863.

[28] S. Richard, O. Colin, C. Angelberger, Towards large eddy simulation of combustion in spark ignition engines, Proc. Combust. Inst. 31 (2007) 3059–3066.

[29] E. Hawkes, R. Cant, A flame surface density approach to large-eddy simulation of premixed turbulent combustion, Proc. Combust. Inst. 28 (1) (2000) 51–58.

[30] S. Candel, T. Poinsot, Flame stretch and the balance equation for the flame surface area, Combust. Sci. Tech. 70 (1990) 1–15.

[31] N. Gourdain, L. Gicquel, M. Montagnac, O. Vermorel, M. Gazaix, G. Staffelbach, M. Garca, J.-F. Boussuge, T. Poinsot, High performance parallel computing of flows in complex geometries part 1: methods, Comput. Sci. Discov. 015003 (2) (2009) 26.

[32] N. Gourdain, L. Gicquel, M. Montagnac, O. Vermorel, M. Gazaix, G. Staffelbach, M. Garca, J.-F. Boussuge, T. Poinsot, High performance parallel computing of flows in complex geometries part 2: applications, Comput. Sci. Discov. 015004 (2) (2009) 28.

[33] C. Lacour, C. Pera, An experimental database dedicated to the study and modelling of cyclic variability in spark-ignition engines with les, SAE Paper 2011-01-1282.

[34] B. Enaux, V. Granet, O. Vermorel, C. Lacour, L. Thobois, V. Dugu, T. Poinsot, Large eddy simulation of a motored single-cylinder piston engine: Numerical strategies and validation, Flow Turb. Combust. 86 (2011) 153–177.

[35] C. Pera, C. Angelberger, Large eddy simulation of a motored single-cylinder engine using system simulation to define boundary conditions: Methodology and validation, SAE Paper 2011-01-0834.

[36] V. Moureau, G. Lartigue, Y. Sommerer, C. Angelberger, O. Colin, T. Poinsot, Numerical methods for unsteady compressible multi-component reacting flows on fixed and moving grids, J. Comput. Phys. 202 (2) (2005) 710–736.

[37] L.-M. Malbec, F. LeBerr, S. Richard, G. Font, A. Albrecht, Modelling turbochard spark-ignition engines: Towards predictive real time simulators, SAE Paper 2009-01-0675.

[38] F. Lafossas, O. Colin, F. L. Berr, P. Menegazzi, Application of a new 1d combustion model to gasoline transient engine operation, SAE Paper 2005-01-2107.

[39] T. Poinsot, S. Lele, Boundary conditions for direct simulations of compressible viscous flows, J. Comput. Phys. 101 (1) (1992) 104–129.

[40] L. Selle, F. Nicoud, T.Poinsot, The actual impedance of non-reflecting boundary conditions: implications for the computation of resonators, AIAA J. 42 (5) (2004) 958–964.

[41] P. Schmitt, T. Poinsot, B. Schuermans, K. Geigle, Large-eddy simulation and experimental study of heat transfer, nitric oxide emissions and combustion instability in a swirled turbulent high-pressure burner, J. Fluid Mech. 570 (2007) 17–417–46.

[42] R. Diwakar, Assessment of the ability of a multidimensional computer code to model combustion in a homogeneous-charge engine, SAE Paper 840230.

[43] V. Moureau, L. Barton, C. Angelberger, T. Poinsot, Towards large eddy simulation in internal-combustion engines: simulation of a compressed tumble flow, SAE Paper 2004-01-1995.

[44] N. Forsythe, N. Muller, Validation of a fluid-structure interaction model for a bileaflet mechanical heart valve, Int. J. Comput. Fluid Dyn. 22 (13) (2008) 541–553.

[45] F. Nicoud, H. B. Toda, O. Cabrit, S. Bose, J. Lee, Using singular values to build a subgrid-scale model for large eddy simulations, Phys. Fluids 23 (2011) 085–106.

[46] H. B. Toda, K. Truffin, G. Bruneaux, O. Cabrit, F. Nicoud, Assessment of subgrid-scale models with a les-dedicated experimental database: pulsatile impinging jet in turbulent cross flow, Phys. Fluids 26 (2014) 075108.

[47] S. Pope, The evolution of surfaces in turbulence, Int. J. Engng Sci. 26 (5) (1988) 445–469.

[48] O. Colin, A. Benkenida, C. Angelberger, 3d modeling of mixing, ignition and combustion phenomena in highly stratified gasoline engines, Oil & Gas Sci. and Tech., Rev. IFP58 (1) (2003) 47–62.

[49] O. Colin, K. Truffin, A spark ignition model for large eddy simulation based on a fsd transport equation (issim-les), Proc Combust Inst 33 (2011) 3097–3104.

[50] J. Duclos, O. Colin, Arc and kernel tracking ignition model for 3d spark-ignition engine calculations, in: COMODIA, Nagoya, 2001, pp. 343–350.

[51] S. Richard, A. Dulbecco, C. Angelberger, K. Truffin, Development of a one-dimensional computational fluid dynamics modeling approach to predict cycle-to-cycle variability in spark-ignition engines based on physical understanding acquired from large-eddy simulation, Int. J. Engine Res. 16 (3) (2015) 379402.

[52] M. Metghalchi, J. Keck, Laminar burning velocity of propane-air mixtures at high temperature and pressure, Combust. Flame 38 (1980) 143–154.

[53] G. Wang, M. Boileau, D. Veynante, K. Truffin, Large eddy simulation of a growing turbulent premixed flame kernel using a dynamic flame surface density model, Combust. Flame 159 (2012) 2742–2754.

[54] G. Woschni, A universally aplicable equation for the instantaneous heat transfer coefficient in the internal combustion engine, SAE Paper 670931.

[55] C. Pera, S. Chevillard, J. Reveillon, Effects of residual burnt gas heterogeneity on early flame propagation and on cyclic variability in spark-ignited engines, Combust. Flame 160 (2013) 1020–1032.

[56] A. Rencher, Methods of Multivariate Analysis, 2nd Edition, J. Wiley & Sons, inc., 2003.

Number of valves	4
Displacement	441 cm^3
Bore	82 mm
Stroke	83.5 mm
Connecting rod length	144 mm
Inlet Valve Open (IVO)	−348 CAD
Inlet Valve Close (IVC)	−142 CAD
Exhaust Valve Open (EVO)	140 CAD
Exhaust Valve Close (EVC)	348 CAD

Table 1: Main characteristics of the SGEmac single cylinder engine. Crank Angle Degrees (CAD) are relative to combustion Top Dead Centre (TDC). Valve timings are given at a reference valve lift of 0.7 mm.

	stab_ref	unstab_dil	unstab_lean
F/A equivalence ratio	1.00	1.00	0.58
Dilution by N_2 (% mass)	0	33	0
IMEP (bars)	3.0	3.1	3.3
Spark timing (CAD)	−20	−50	−52
Engine speed (rpm)	1200	1200	1200

Table 2: Characteristics of the three simulated fired operating points stab_ref, unstab_dil and unstab_lean of the SGEmac database.

Tables

	Experiment	**LES**
Number of cycles	100	10
Mean trapped mass (mg)	179.7	179.5
COV(trapped mass) (%)	0.2	0.1
Mean IMEP (bar)	3.0	3.1
COV(IMEP)(%)	1.1	0.9
Mean p_{max} (bar)	19.7	19.8
COV(p_{max})(%)	4.7	3.9

Table 3: Cycle averaged mean and variability of engine parameters for the stable stab_ref case.

	unstab_dil		**unstab_lean**	
	Experiment	**LES**	**Experiment**	**LES**
Number of cycles	200	28	200	28
Mean trapped mass (mg)	259	259.2	277	280.4
COV(trapped mass) (%)	0.1	0.1	0.3	0.1
Mean IMEP (bar)	3.1	2.9	3.3	3.1
COV(IMEP)(%)	7.6	9.1	8.2	8.1
Mean p_{max} (bar)	16.4	16.2	18.9	19.2
COV(p_{max})(%)	12.5	12.9	14.5	13.8
Mean CA2 (deg.)	−7.3	−8.0	−7.9	−9.1
COV(CA2) (%)	5.2	6.3	5.9	6.4
Mean CA50 (deg.)	21.3	20.5	19.0	16.6
COV(CA50) (%)	7.6	8.5	7.7	8.3

Table 4: Cycle averaged mean and variability of engine parameters for the unstable unstab_dil and unstab_lean cases.

y / x	$\overline{S}_L$	$\widetilde{T}_{spk}$	$\widetilde{Y}_{dil,spk}$	τ_{dil}	τ_{res}	$\widetilde{\Phi}_{spk}$	$\widetilde{\Phi}$
mean(x)	0.23m/s	549 K	0.39	39.1%	7.3%	1	1
2σ (in %)	(8.6%)	(1.1%)	(2%)	(1.2%)	(1.5%)	0%	(0%)
$\overline{S}_L$	1	-0.42	-0.93	-0.84	0.41	N.A.	N.A.
$\widetilde{T}_{spk}$	-0.42	1	0.59	0.52	-0.51	N.A.	N.A.
$\widetilde{Y}_{dil,spk}$	-0.93	0.59	1	-0.9	-0.48	N.A.	N.A.
τdil	-0.84	0.52	-0.9	1	-0.28	N.A.	N.A.
τ_{res}	0.41	-0.51	-0.48	-0.28	1	N.A.	N.A.
$\widetilde{\Phi}_{spk}$	N.A.	N.A.	N.A.	N.A.	N.A.	N.A.	N.A.
$\widetilde{\Phi}$	N.A.	N.A.	N.A.	N.A.	N.A.	N.A.	N.A.

Table 5: Correlations coefficients R between several local and global thermodynamic variables at ignition timing in the diluted case.

y / x	$\overline{S}_L$	$\widetilde{T}_{spk}$	$\widetilde{Y}_{dil,spk}$	τ_{dil}	τ_{res}	$\widetilde{\Phi}_{spk}$	$\widetilde{\Phi}$
mean(x)	0.26m/s	515.5 K	0.05	5.1%	7.6%	0.56	0.56
2σ (in %)	(3.9%)	(1.24%)	(13.69%)	(7%)	(3.2%)	(1%)	(0.7%)
$\overline{S}_L$	1	0.77	-0.72	-0.61	0.32	0.71	0.6
$\widetilde{T}_{spk}$	0.77	1	-0.4	-0.29	0.59	-0.1	0.033
$\widetilde{Y}_{dil,spk}$	-0.72	-0.4	1	0.58	-0.29	-0.54	-0.39
τ_{dil}	-0.61	-0.29	0.58	1	-0.29	-0.63	-0.87
τ_{res}	0.32	0.59	-0.29	-0.29	1	-0.16	-0.001
$\widetilde{\Phi}_{spk}$	0.71	-0.1	-0.54	-0.63	-0.16	1	0.76
$\widetilde{\Phi}$	0.6	0.033	-0.39	-0.87	-0.001	0.76	1

Table 6: Correlations coefficients R between several local and global thermodynamic variables at ignition timing in the lean case.

Sources = variation of :	**Effect on spark-ignition**		
	unstab_lean	**unstab_dil**	**Ozdor et al. [1]**
Global A/F ratio ϕ	++	N.A.	++
Global dilution τ_{dil}	++	++	++
Spatial inhomogeneities ϕ_{spk}^{inhom} **and** T_{spk}^{inhom}	+	-	+ to +++
Flow $(w/u)_{spk}$, $\lvert U\rvert_{spk}$	+++	++	+++
Sources = variation of :	**Effect on the main propagation phase**		
	unstab_lean	**unstab_dil**	**Ozdor et al. [1]**
In-cylinder charge m_{fu}	++	++	+++
Global A/F ratio ϕ	++	N.A.	++
Global dilution τ_{dil}	++	++	++
Flow E_{T_y}	-	+	++

Table 7: Qualitative impact of different sources of CCV for the studied lean and diluted case: first those impacting the spark-ignition, second those impacting the main propagation phase are listed. The meaning of the symbols is as follows: +++: very strong correlation with ($|R| > 0.7$ for our LES findings), ++: moderate correlation ($|R| > 0.5$ for our LES findings), +: weak correlation ($|R| \approx 0.4$ for our LES findings), -: no measurable impact and N.A. : not applicable.

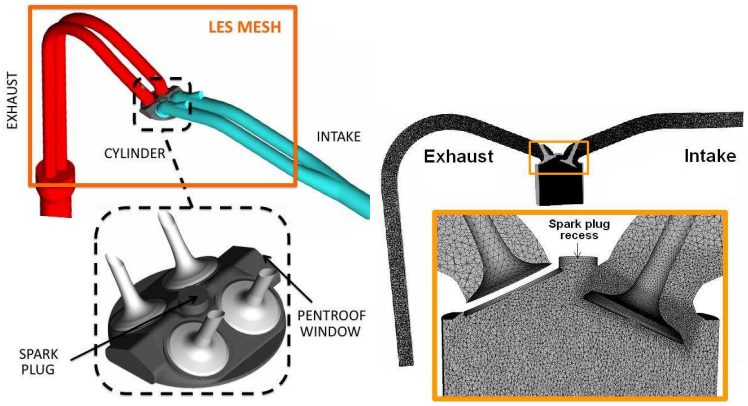

(a) (b)

Figure 1: (a) Computational domain for the LES (rose frame), including the combustion chamber and a part of the intake and exhaust ducts; (b) View of the tetrahedral mesh during the intake stroke (−290 CAD).

Figures

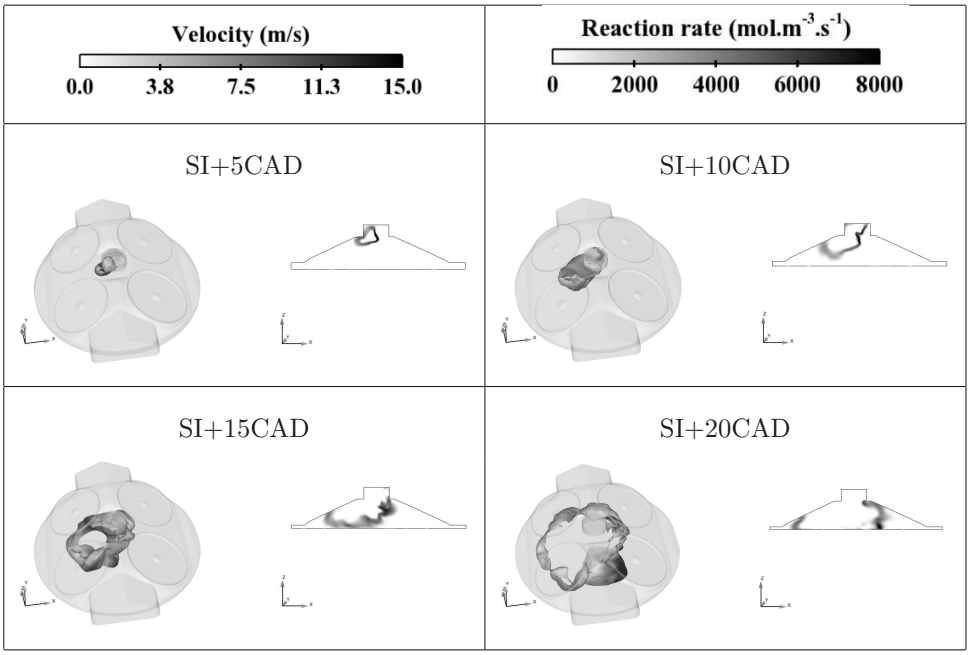

Figure 2: Visualisation of the flame for an individual engine cycle and at 4 crank angles. For each angle the left plot shows a top view of the chamber with an iso-surface of the reaction rate coloured by the flow velocity, while the right shows a plot of the reaction rate field in a vertical plane of the chamber.

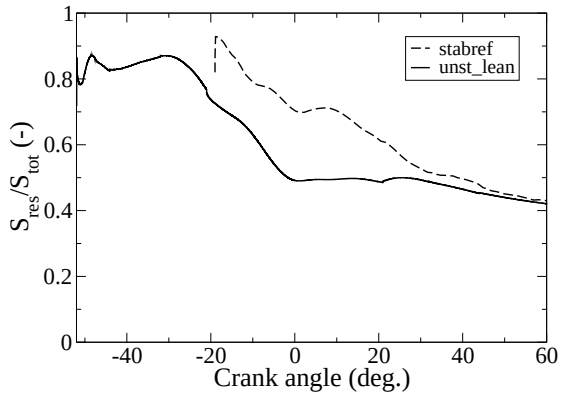

Figure 3: Time evolutions of the ratio between the resolved and the total flame surface for a selected individual cycle of stab_ref and of stab_lean cases.

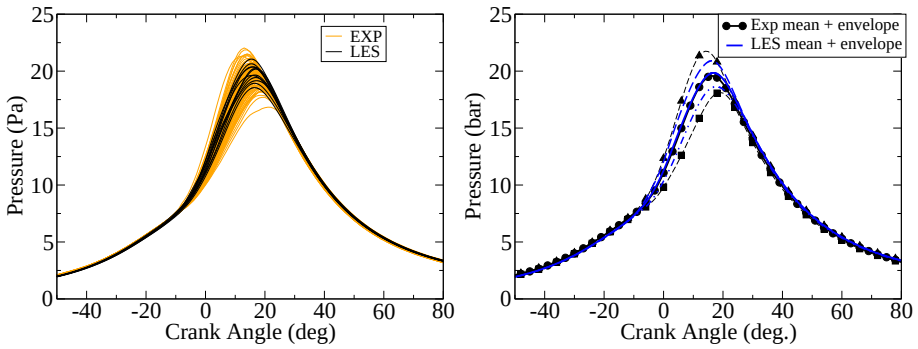

(a) Individual cycles (b) Statistical comparison

Figure 4: Comparisons of the time evolutions of the cylinder pressure predicted by LES with experimental findings for the stab_ref case.

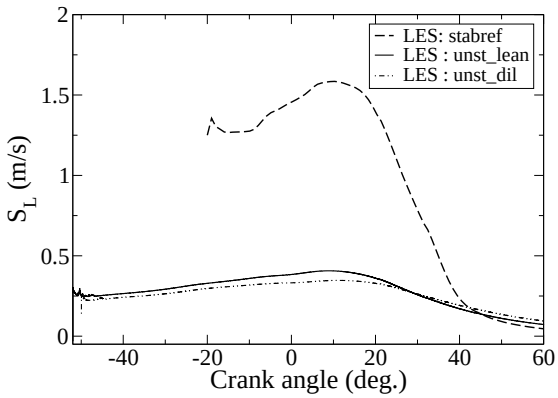

Figure 5: Time evolutions of the phase averaged laminar flame speeds extracted from the LES of the three studied cases of the SGEmac database.

Figure 6: Visualisation of the flame surface using an iso-surface of the reaction rate (50 mol.m^{-3}.s^{-1}) coloured by the velocity (blue: 0m/s, red: 20m/s) 35 CA degrees after ignition for 6 consecutive cycles of unstab_dil.

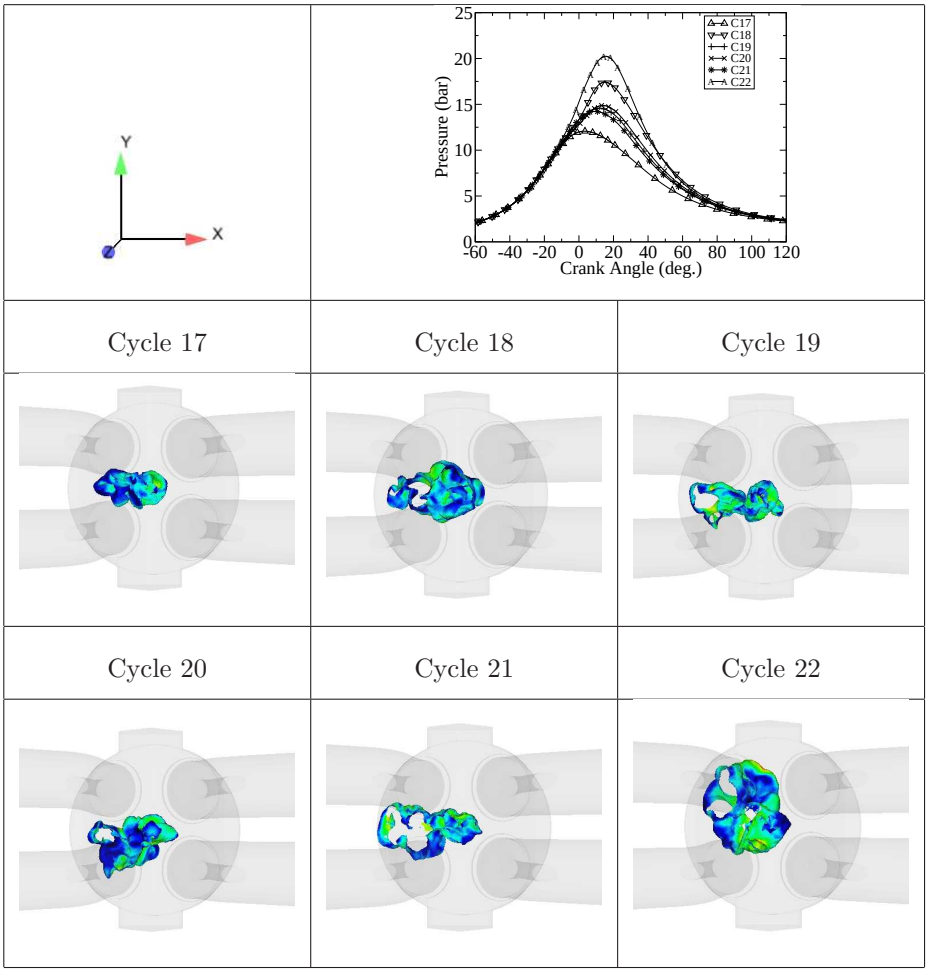

Figure 7: Visualisation of the flame surface using an iso-surface of the reaction rate (50 mol.m^{-3}.s^{-1}) coloured by the velocity (blue: 0m/s, red: 20m/s) 35 CA degrees after ignition for 6 consecutive cycles of unstab_lean.

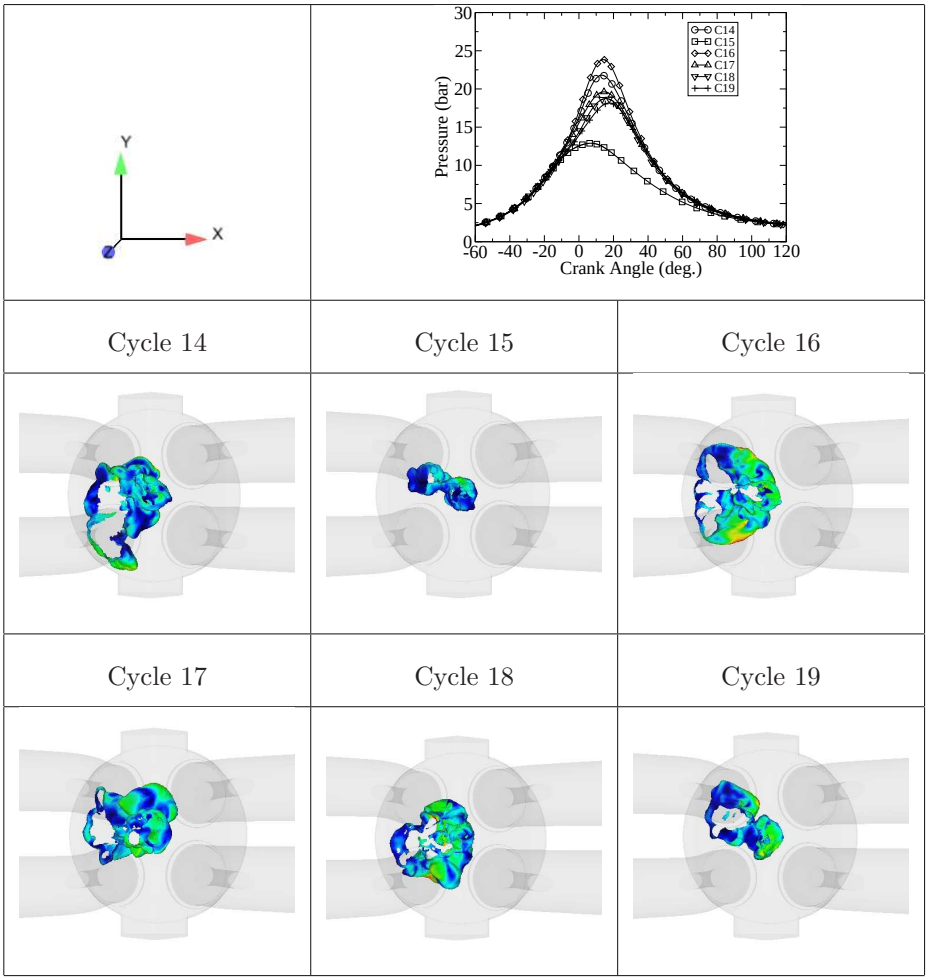

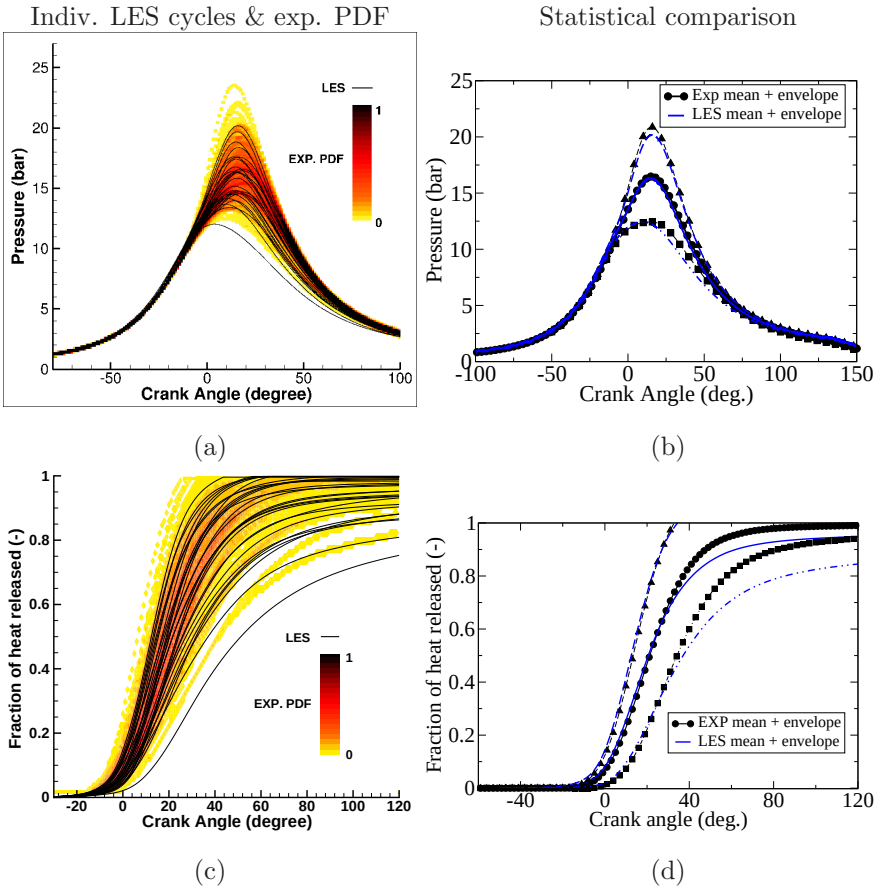

Figure 8: Comparison of the time evolutions of cylinder pressure and fuel mass fraction burnt (energetic) predicted by LES with experimental findings for the unstab_dil case.

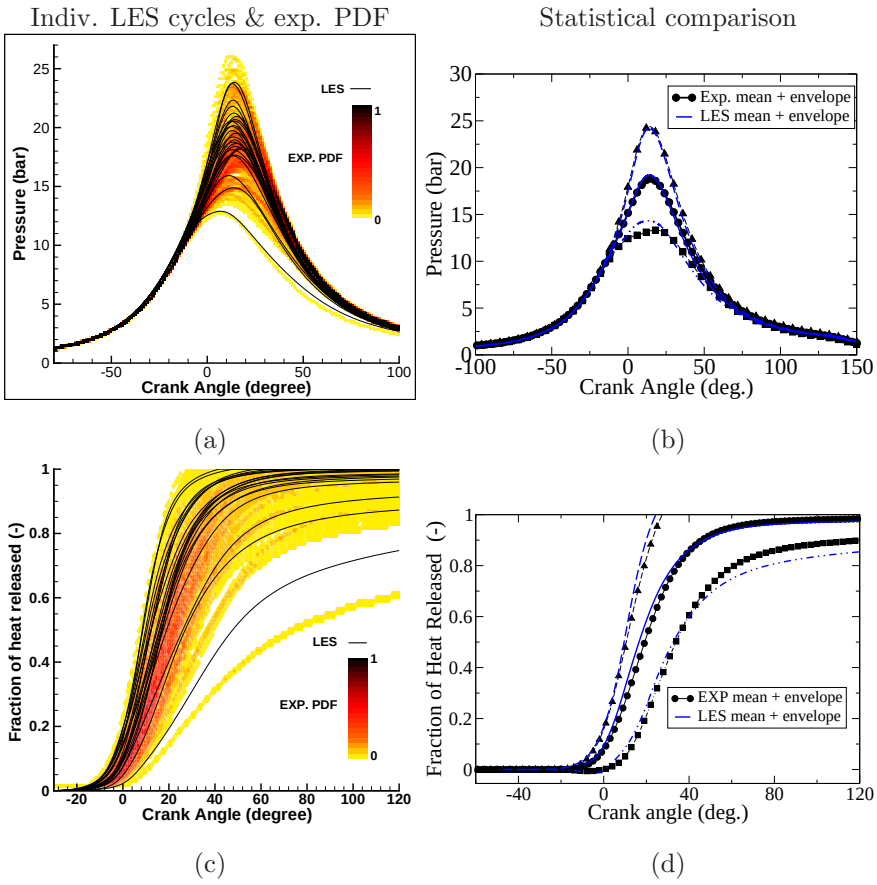

Figure 9: Comparison of the time evolutions of cylinder pressure and fuel mass fraction burnt (energetic) predicted by LES with experimental findings for the unstab_lean case.

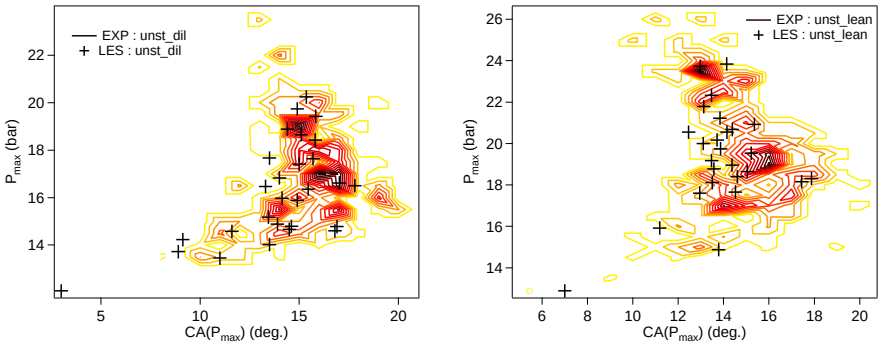

(a) unstab_dil (b) unstab_lean

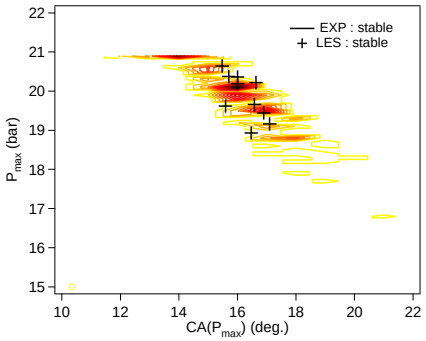

(c) stab_ref

Figure 10: Matekunas diagrams for the three studied cases.

Figure 11: Comparison of the flame propagation of a fast (C9) and a slow (C17) cycle of the unstab_dil case. Left: vertical central cut showing the instantaneous reaction rate fields at four instants during the combustion phase. Right : crank angle evolutions of the fresh gas velocity components along the flame front (axial $< \widetilde{u}|_{\widetilde{c}=0.001} >$ and vertical $< \widetilde{w}|_{\widetilde{c}=0.001} >$) following Eq. (10).

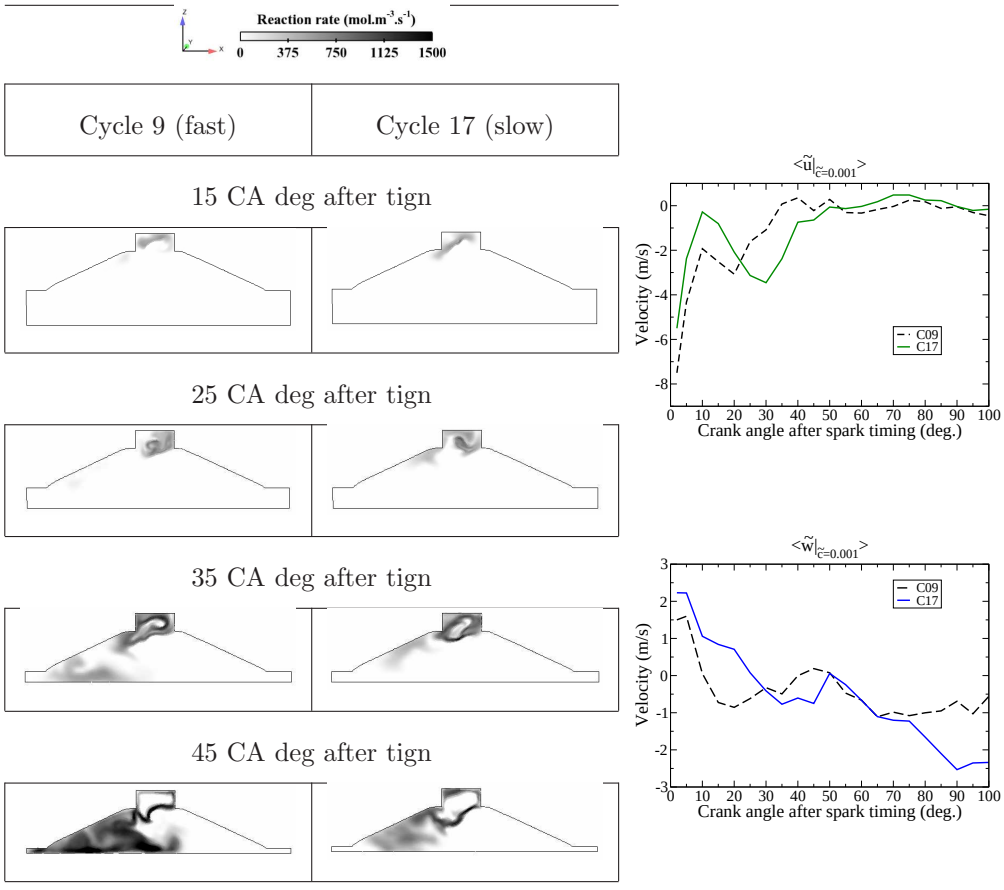

Figure 12: Comparison of the flame propagation of a fast (C18) and a slow (C21) cycle of the unstab_lean case. Left: vertical central cut showing the instantaneous reaction rate fields at four instants during the combustion phase. Right : crank angle evolutions of the fresh gas velocity components along the flame front (axial $< \widetilde{u}|_{\widetilde{c}=0.001} >$ and vertical $< \widetilde{w}|_{\widetilde{c}=0.001} >$) following Eq. (10).

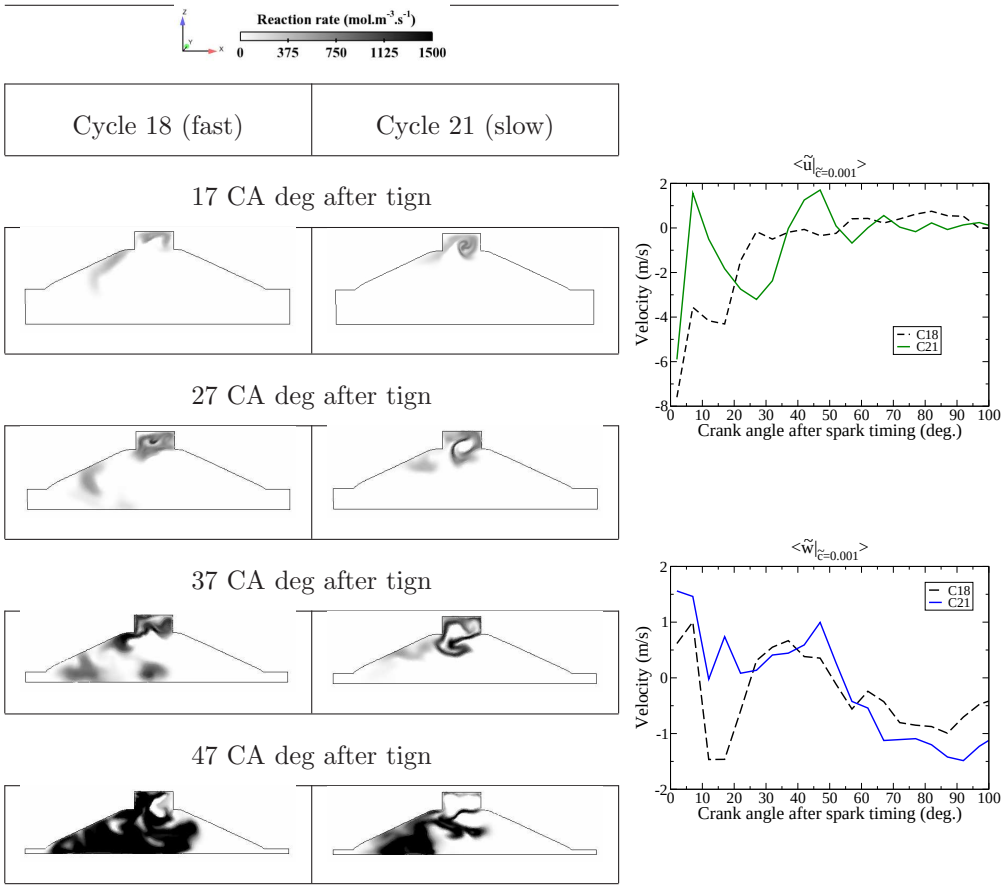

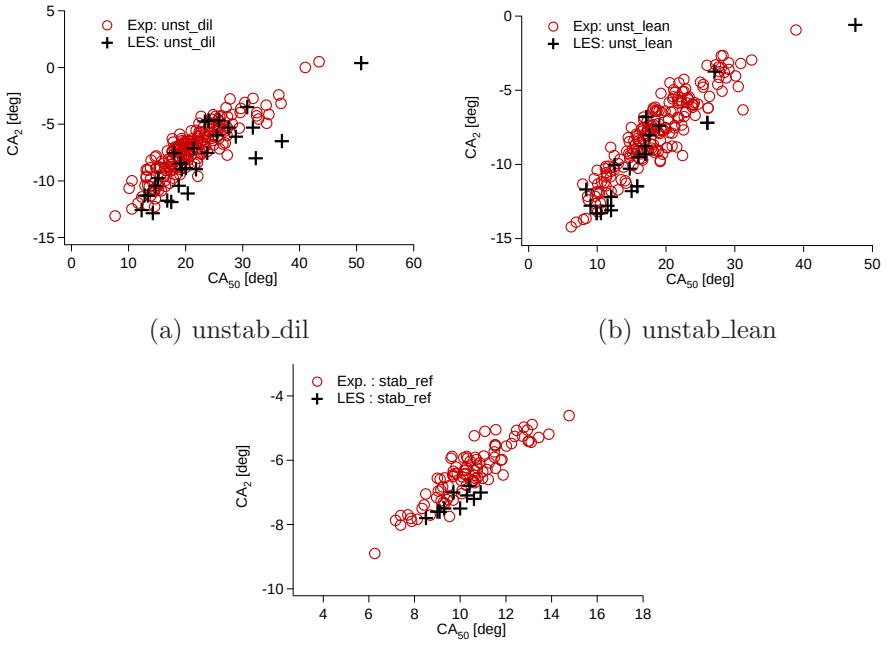

(a) unstab_dil (b) unstab_lean

(c) stab_ref

Figure 13: Comparisons between experimental and LES correlations between CA2 and CA50.

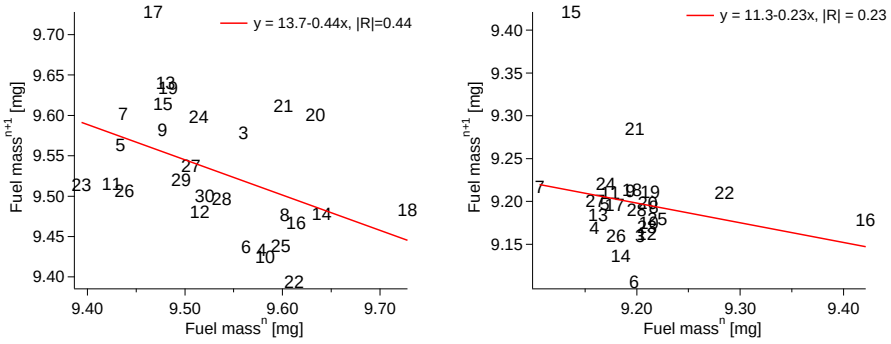

(a) unstab_dil (b) unstab_lean

Figure 14: Scatter plot of the enclosed mass of fuel (bottom) of the subsequent cycle $(n+1)$ as a function of cycle (n).

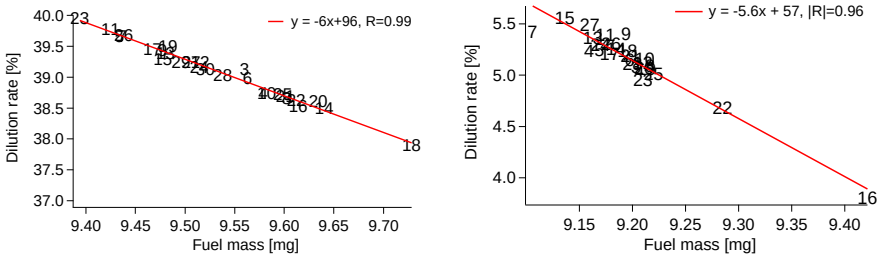

(a) unstab_dil (b) unstab_lean

Figure 15: Scatter plot of the dilution rate as a function of the enclosed mass of fuel.

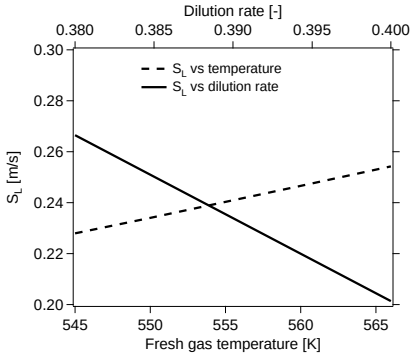

Figure 16: Evolution of the laminar flame speed as function of the temperature and of the dilution rate for the conditions encountered at ignition timing in the diluted case.

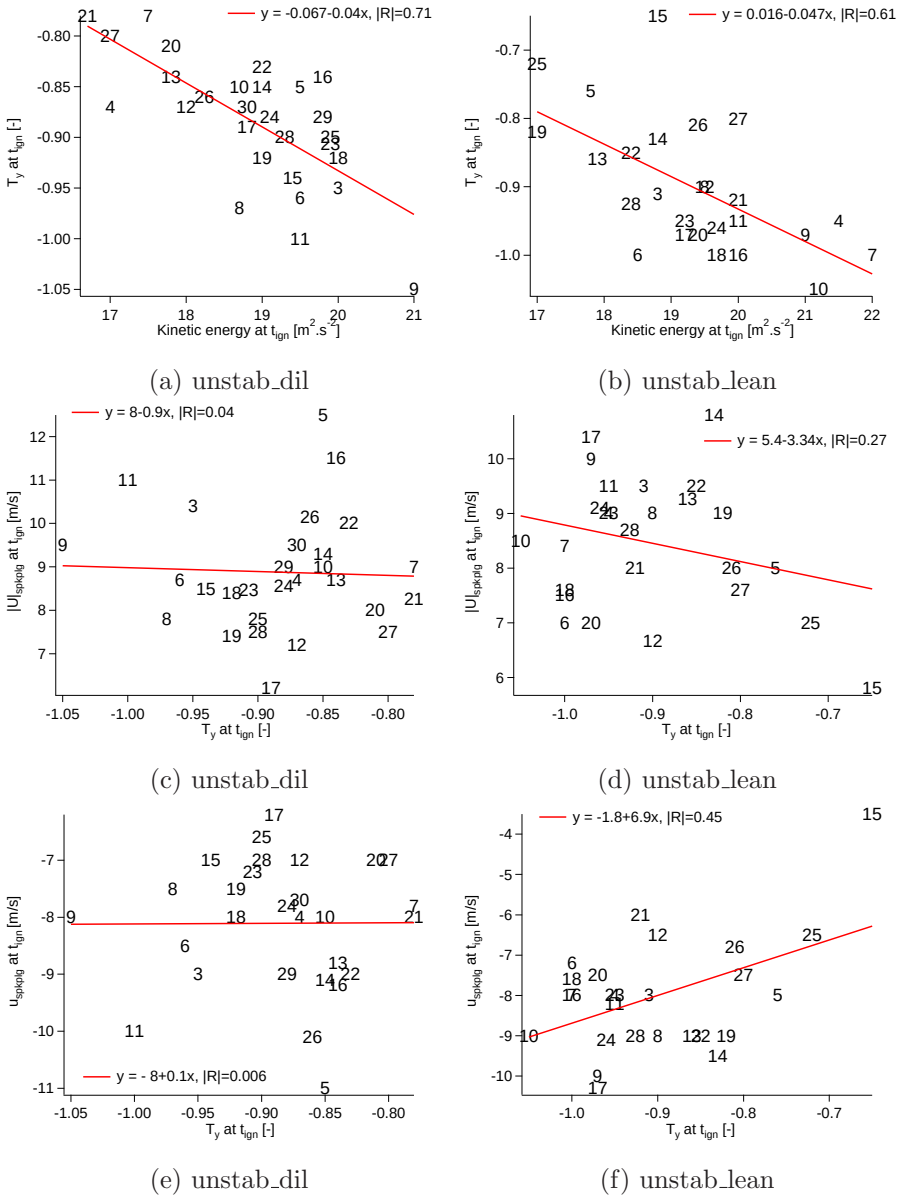

Figure 17: Scatter plot of the tumble number as a function of the average in-cylinder resolved kinetic energy (top), of the resolved velocity magnitude (middle) and of the axial velocity (bottom) in the vicinity of the spark plug at ignition timing.

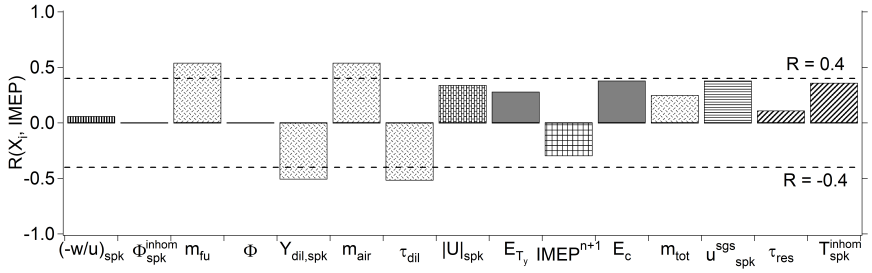

(a) unstab_dil

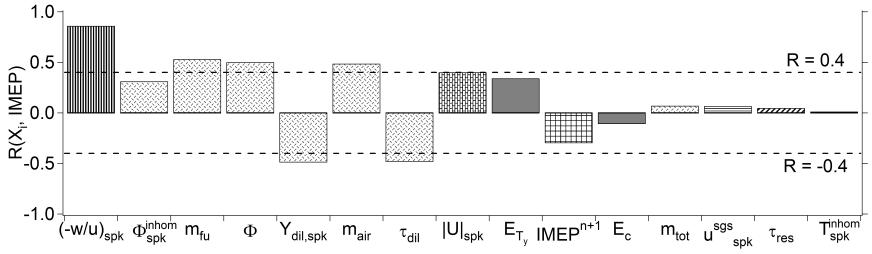

(b) unstab_lean

Figure 18: Histogram of correlation coefficients between the IMEP and each variable X_i (listed below the abscissa) obtained from LES results using single linear regression models in the diluted case a) and in the lean case (b). Similar patterns filling the bars indicate variables which are correlated to each other.

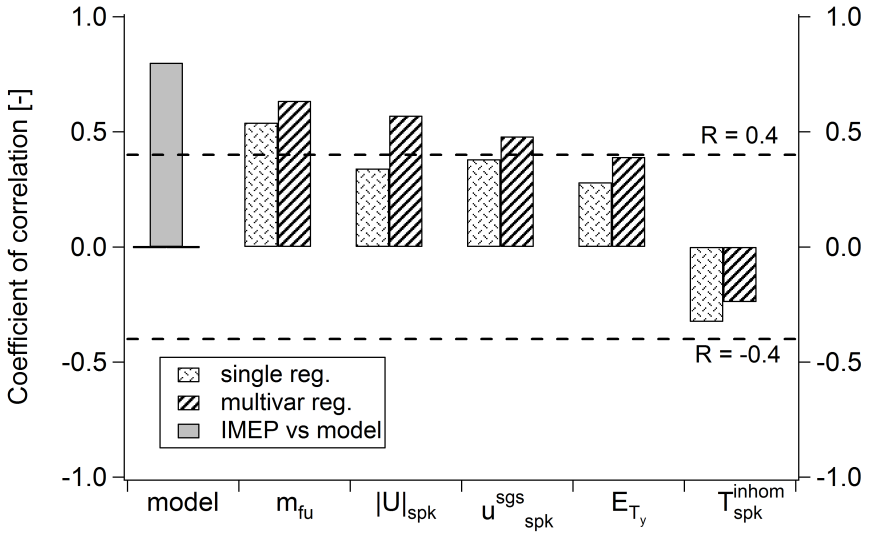

Figure 19: Correlation coefficients obtained from LES results in the diluted case. The first bar on the left gives the correlation coefficient between IMEP and the obtained best fitting model IMEP^{model}. Bars filled with dots (the left ones) indicate correlation coefficients obtained between the $\widetilde{X}_k$ and IMEP via the single regression model. Bars filled with lines (the right ones) indicate the correlation coefficients from the multivariate analysis between the independent variables $\widetilde{X}_k$ and IMEP-$\sum_{i \neq k} \beta_i \widetilde{X}_i(n)$.

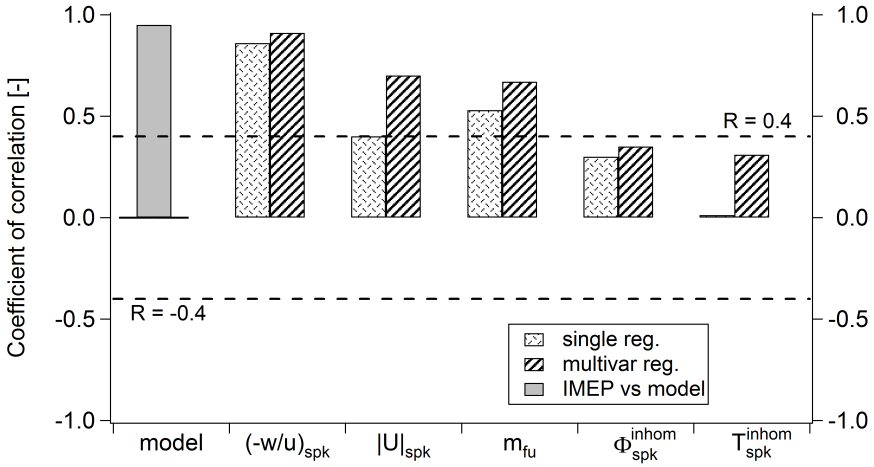

Figure 20: Correlation coefficients obtained from LES results in the lean case. The first bar on the left gives the correlation coefficient between IMEP and the obtained best fitting model IMEP^{model}. Bars filled with dots (the left ones) indicate correlation coefficients obtained between the $\widetilde{X}_k$ and IMEP via the single regression model. Bars filled with lines (the right ones) indicate the correlation coefficients from the multivariate analysis between the independent variables $\widetilde{X}_k$ and IMEP-$\sum_{i\neq k}\beta_i\widetilde{X}_i(n)$.